Geophysical Journal International

Geophys. J. Int. (2022) **228,** 2018–2037
Advance Access publication 2021 November 15
GJI Seismology

https://doi.org/10.1093/gji/ggab458

Stress drops of hydraulic fracturing induced microseismicity in the Horn River basin: challenges at high frequencies recorded by borehole geophones

Adam G. Klinger and Maximilian J. Werner

School of Earth Sciences, University of Bristol, Wills Memorial Building, Queen's Road, Bristol, BS8 1RJ, UK. E-mail: ak13671@bristol.ac.uk

Accepted 2021 November 2. Received 2021 November 2; in original form 2021 August 26

SUMMARY

The ground motions caused by seismicity associated with fluid injection can pose a significant hazard. Borehole geophone arrays can provide access to tiny seismic events, which can extend the investigated magnitude range. However, the high frequency phase arrivals (i.e., >100 Hz) also present challenges associated with high frequency cut-offs (f_{max}), stronger attenuation and resonances within geophones. These effects limit our ability to accurately constrain attenuation models and high frequency source parameters. We investigate 112 $-0.6 \leq M_w \leq 0.7$ seismic events and calculate corner frequencies and stress drops from 90 of these events recorded during hydraulic fracturing treatment in the Horn River basin, British Columbia. High frequency resonances (>250 Hz) caused by spurious frequency excitation and/or coupling issues can significantly distort the shape of phase arrival spectra and affect source parameter estimates. Critically, resonances vary in strength between (nearly) colocated events, which may compromise the validity of a spectral ratio approach. For stations showing the cleanest spectra, the Brune model provides a decent fit to the displacement spectra. However, bandwidth limitations, low signal-to-noise ratios, high frequency cut-offs and significant attenuation still hinder our ability to retrieve high frequency source parameters. We find that a frequency independent $Q_p = 180 \pm 40$ provides a reasonable model for crustal attenuation but the large uncertainty caused by resonances prevents a robust constraint. From those events that show the best fits, we find a mean Madariaga corner frequency of 210 Hz ± 30 from *P*-phase arrivals, which is in the range of expected values if self-similarity extends into negative magnitudes. We also calculate a mean stress drop of 1.6 MPa ± 1.2, which is within the tectonic range but slightly lower than other deeper regional studies, which can be explained by lower effective stresses and/or a lower crustal shear strength. We find no evidence for a change in stress drop with depth or distance from the point of injection. A plausible explanation is that effective stresses are lowered relatively quickly over the entire fault zone via direct hydraulic connections. However, the large uncertainties make it difficult to interpret source parameter variability in detail. For high resolution monitoring and source properties of microseismicity, there is an urgent need for high quality high frequency recordings unaffected by spurious frequencies.

Key words: Earthquake source observations; Induced seismicity; Seismic attenuation; Seismic instruments.

1 INTRODUCTION

In recent years, subsurface industrial activity has increased in both renewable and non-renewable energy sectors. Hydraulic fracturing (e.g., Clarke *et al.* 2014), enhancement of geothermal systems (e.g., Deichmann & Giardini 2009; Holmgren & Werner 2021), carbon capture and storage (e.g., Verdon *et al.* 2013) and waste water injection (e.g., Keranen *et al.* 2014) have demonstrated the ability to cause felt seismicity. This study focuses on seismicity induced by hydraulic fracturing, which in most cases is not felt (Rubinstein & Mahani 2015), but via the re-activation of pre-existing faults can induce damaging earthquakes (e.g., Lei *et al.* 2017; Tan *et al.* 2020). To mitigate the seismic risk linked to fluid injection, we need to better understand the physical mechanisms causing induced seismicity and how the mechanisms vary between data sets. Some authors suggest direct hydraulic pressure dominates as the main mechanism,

while others posit diffusion of pore-pressure fluids (e.g., Goebel *et al.* 2017; Goebel & Brodsky 2018), aseismic slip (Eyre *et al.* 2019) or stress transfer due to the opening of hydraulic fractures (Kettlety *et al.* 2020).

The spatio-temporal analysis of microseismic event locations is fundamental to understanding how fracture networks develop. To understand how the rupture physics are related to the injection of fluids, however, source properties (e.g., moment tensors, moment magnitude and stress drop) are needed. Stress drop is a particularly insightful metric because it is a function of two physical attributes: seismic moment (M_o) and corner frequency (f_c). Seismic moment is related to the rupture size and slip; corner frequency is the curvature change point on a displacement spectrum that can be interpreted, using the model of Madariaga (1976), as related to rise time and finite propagation length (Aki & Richards 2002). In enhanced geothermal systems, some studies have found that the stress drop can be used as a proxy for the pore-fluid pressure (Pearson 1981; Allmann *et al.* 2011; Lengliné *et al.* 2014). These studies suggest stress drops decrease nearer to the point of injection as a result of a lower effective stress.

Stress drops can be used to better understand the scaling of high frequencies for different M_w's , which is also important when developing ground motion prediction equations. Many tectonic studies support the geometrical similarity of tectonic earthquakes implicit in the canonical model for far-field radiation (e.g., Abercrombie 1995; Hiramatsu *et al.* 2002; Ide *et al.* 2003; Allmann & Shearer 2009). However, it is still debated as to whether self-similarity is also applicable to microseismicity (Ide *et al.* 2004; Venkataranman *et al.* 2006; Lin *et al.* 2016).

Source parameters from microseismicity are particularly difficult to accurately determine because of unaccounted attenuation under the assumption of frequency-independent anelastic attenuation and bandwidth limitations. Unaccounted attenuation has also been observed in the form of a high frequency cut-off (Hanks 1982), often termed f_{max}, which led to the introduction of κ (Anderson & Hough 1984). However, the physical meaning behind κ remains to be established. Most studies attribute κ to a shallow crustal site effect (Ktenidou *et al.* 2014) but it might also manifest in borehole environments (Ide *et al.* 2003). Others have used a frequency dependent Q and argued that it is particularly needed for source parameter estimation along boreholes (Ide *et al.* 2003). Bandwidth limitations can also cause spurious scaling of apparent stress with magnitude, as shown by Ide & Beroza (2001), due to an underestimation of radiated energy.

Stress drops also allow us to better understand how the underlying physics may differ between deeper, tectonic settings and shallower induced settings. Some studies suggest similar stress drops in induced and tectonic environments (e.g., Tomic *et al.* 2009; Yenier & Atkinson 2015; Abercrombie 2015; Huang *et al.* 2016; Zhang *et al.* 2016; Ruhl *et al.* 2017; Holmgren *et al.* 2019) whereas others find differences (e.g., Hua *et al.* 2013; Lengliné *et al.* 2014; Hough 2014). It may also be important to account for the faulting style and depth of the events when interpreting the differences in stress drop between tectonic and induced data sets (Huang *et al.* 2017).

In recent years, the empirical Green's function (EGF) method and spectral decomposition method (Trugman & Shearer 2017) have been used widely to determine stress drop (Shearer *et al.* 2019). Both methods attempt to remove path and receiver effects using deconvolution from a far-field signal, which presumes a form of linearity of these effects. The EGF method, in particular, can show biased estimates of the target event corner frequency based on the smaller event corner frequency (Abercrombie 2015; Shearer *et al.* 2019). EGFs must be smaller than the targets, therefore finding suitable EGFs for microseismic events is limited by the poorer signal-to-noise ratio (SNR) from already very small events. As such, it can be difficult to generate a comprehensive catalogue of stress drop values using the spectral ratio approach in a microseismic data set. Practically, picking an EGF requires more time compared to directly fitting a source model, which can be done in real time. For these reasons, there is still a need to understand the far-field spectra and identify features that could compromise more sophisticated approaches, such as the high frequency resonances documented here.

For source parameter estimation, it is useful to have seismic data from both surface and borehole data. Downhole data show arrivals with a higher SNR, reduced surface attenuation effects and vast catalogues of microseismic events. However, downhole geophones can record resonances that are less likely to occur at surface seismometers. At the receiver these are: low frequency plane waves propagating through the fluid in a wellbore (Sun & McMechan 1988); high frequency dispersive waves propagating along the pipe-interface, also known as Stoneley waves (Haldorsen *et al.* 2006); reverberations in the casing and coupling issues (Gaiser *et al.* 1988). At the event source side, resonances can be caused by fluid-filled cracks (Aki *et al.* 1977) and small undetected events (e.g., Pettitt *et al.* 2009). Along the path, waves can be trapped within reflecting layers (waveguides) especially when there are alternating layers of sandstone and shales (e.g., Van Der Baan 2009). In addition to all these effects, downhole geophones can show spurious resonances caused by the movement of the geophone system orthogonal to the normal working axis (Faber & Maxwell 1997).

The objective of this study is to calculate stress drops from microseismicity at one of the plays within the Horn River basin, one of the largest unconventional reservoirs for gas-trapped shales in North America (Yoon *et al.* 2018). Previous studies have used this data set to conduct statistical modelling (Verdon & Budge 2018), elasto-static stress transfer modelling (Kettlety *et al.* 2019), and to study shear wave splitting (Baird *et al.* 2017). Here, we first show examples of amplifications in the pre-event noise and phase arrivals from a sub-catalogue of 112 events which are selected according to quality criteria from a vast data set of 90 000+ events. These high frequency amplifications are most likely caused by coupling issues and the excitation of spurious resonances in the instruments. Secondly, we calculate M_w estimates and determine a crustal attenuation model. Thirdly, we test the depth and distance dependence of stress drop from a single injection point (e.g., Allmann *et al.* 2011) by focusing on 90 of the 112 events linked to injection at stage A14, where microseismicity illuminates a fault zone (Verdon & Budge 2018; Kettlety *et al.* 2019). For these 90 events, we estimate corner frequency and stress drop. Our results add further evidence that self-similarity extends down to negative magnitudes and that the absolute stress drop values are within the tectonic range. We also find no correlation between stress drop and depth or distance from the point of injection. Unfortunately, corner frequency and stress drop estimates have a large uncertainty, which makes it difficult to infer statistically significant physical correlations.

2 DATA

We use data acquired by a contractor during hydraulic-fracturing operations in the Horn River basin, British Columbia. There are three stratigraphic units that were targeted during operations: The Muskwa, Otter Park and Evie formations. These are all fine-grained,

organic rich shales that likely formed in an open marine environment (Yoon *et al.* 2018).

The contractor used a multiwell, multistage approach to stimulate fractures in the shale formation in the Horn River basin. 10 wells were drilled and 237 stages were completed using a toe-heel zipper frack technique. During operations, the contractor recorded continuous seismic data and provided us with continuous SEG-D tapes recorded using 15 Hz GEO-OMNI-2400 borehole geophones at 2 arrays (K and S), each with 35 stations, as shown in Fig. 1. The instrument response, as determined from the lab, shows the amplitude of the output increases up to the natural frequency (15 Hz), after which the instrument dampening enables a flat response up to at least 500 Hz with an output of 1.1 volts per inch per second. Instrument specifications also mention that spurious frequencies are expected at frequencies greater than 365 Hz. The instrument samples at 4000 Hz. The contractor also provided us with original station orientations determined from perforation shots. The *Z* component is mostly aligned in the direction of the well at both the K- and S-well, while the first and second components are subhorizontal.

The K-well geophones were deployed at 1215–1695 m and the S-well geophones between 1193 and 1663m with 13–15 m spacing between geophones. We were also provided with a catalogue of more than 90 000 moment magnitudes ($-3 < M_w < 0.55$), stress drops, fault radii and locations for all events and full moment tensor inversions for 35 per cent of events. The methods used for determining source parameters were not available, nor their uncertainties. For this reason, we recalculate corner frequencies and stress drops. We also recalculate M_w estimates in Section 4.2. From here on magnitudes provided by the contractor are denoted by $M_{w,c}$ and estimates from this study are denoted as M_w.

Previous research shows that the stimulation of stage 14 in well A (stage A14) resulted in microseismicity that extended into the basement rock, indicating fault reactivation (Kettlety *et al.* 2019). The microseismicity is usually largest underneath the play, and therefore of particular interest from a seismic hazard perspective. We can also test the hypotheses relating stress drop to depth or distance form an injection point by limiting stress drop analysis to events linked to stage A14 (Fig. 1b), which we implement in Section 5.5.

2.1 Velocity model and locations

The contractor also provided us with the event locations and velocity model (Fig. 2). The velocity model was initially determined using a tapered sonic log to show shale transitions. It was then calibrated using perforation shots assuming elliptical anisotropy. Relative locations of seismic events were then improved by using double difference relocation (Waldhauser & Ellsworth 2000). Uncertainty is estimated at ±50 m for relative locations and ±110 m for absolute locations (Kettlety *et al.* 2019).

2.2 Traveltimes

We use a finite-difference approach to solve the eikonal equation (Podvin & Lecomte 1991) using NonLinLoc (Lomax *et al.* 2009). In doing so, we calculate the fast traveltimes to each grid point over a 2-D matrix to construct traveltime lookup tables for the *P*- and *S*-phase arrivals. We then use the locations provided in the catalogue to calculate the geometric distance between source and receiver and interpolate the look-up table to calculate traveltimes for each station.

2.3 Data and results availability

Although operator-provided data are not currently available publicly, we provide an open-access data set of our results on Zenodo (Klinger & Werner 2021). The spreadsheet contains event IDs, magnitudes, corner frequencies and stress drops as well as their uncertainties of the 94 events analysed in Section 5.5. The data may be useful for testing the replicability of our conclusions with other data sets or to compare stress drops.

3 PROCESSING

The contractor provided us with ∼9 hr of raw SEG-D data from the period of operation separated into 20-min files. Baird *et al.* (2017) then separated out the continuous data into event separated SAC files using times from the catalogue, and also rotated stations into NEZ orientation. Over 90 000 detected events were provided by the contractor, though individual phase picks for each station were not provided. We pick the data using an STA/LTA method (Allen 1978) and require accurate phase arrival picks across all stations—a condition only met by high SNR events. From visual inspection, we find that an STA/LTA = 15 is required for the *P* phase and an STA/LTA = 30 for the *S* phase. The higher threshold for the *S* phase is due to the higher pre-phase arrival noise (the *P*-wave coda). To improve the pick accuracy we also apply a 4-pole, 2 pass Butterworth filter between 15 Hz (natural frequency) and 200 Hz.

As the instrument response is 1.1 volts per inch per second, we correct for this by: dividing the time-series by 1.1, unit converting from inches to metres and integrating to displacement. We then find the polarization angle of the radial component for each event by calculating the covariance matrix of the 3 components on the primary arrival using a 0.1 s time window that captures the full phase and some coda. We then rotate the vertical component to the vector which corresponds to the maximum eigenvalue. For the SH and SV components, the covariance matrix is calculated from the second phase arrival. We then rotate the north and east components using the eigenvalue that maximises transverse particle motion.

3.1 Multitaper transformation

We use the multitaper method to transform from the displacement–time series to a displacement–frequency spectrum in line with many other source studies (e.g., Allmann & Shearer 2009; Harrington *et al.* 2015; Wu & Chapman 2017; Holmgren *et al.* 2019). The multitaper method reduces the amount of sidelobe leakage from lower frequencies (Gubbins 2005), which increases the accuracy of transformation compared to a standard Fourier transform. We use the following equation:

$$S(f) = |\sum_{t=0}^{n-1} x(t)a(t)e^{-2\pi i f t}|^2, \quad (1)$$

where $S(f)$ is the power spectral density function, $a(t)$ is a series of weights, $x(t)$ is the signal, f is frequency and t is time, n is the number of data points in a time-series. The user is required to assign the time-bandwidth product (TBW) and the number of tapers (k). The TBW is the averaging bandwidth for each spectral point estimation. k refers to the Slepian sequence of orthogonal, prolate tapers used to weight the time series (Prieto *et al.* 2007). It is still uncertain what the optimal choices for these parameters are.

From a displacement time series, the units of the power spectrum are in $m^2\ Hz^{-1}$. Therefore, to convert to displacement amplitude we

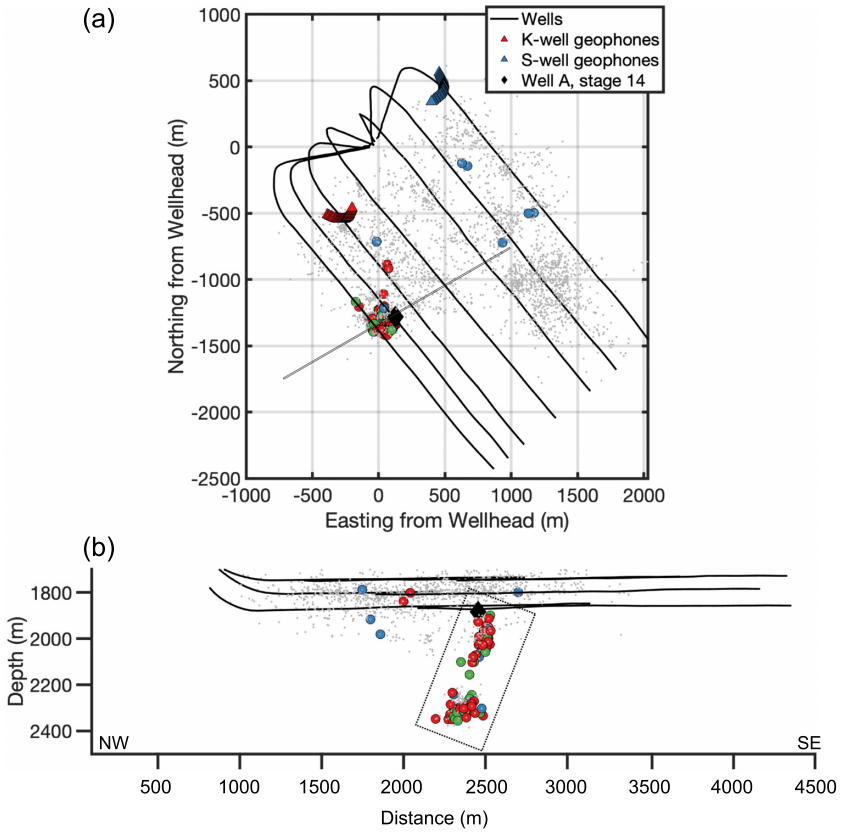

Figure 1. (a) Map and (b) Cross sectional view along the grey line in (a) illustrating the multiwell hydraulic fracturing operation, monitoring wells and locations of induced seismicity. The coloured events correspond to those that meet processing criteria. Circles denote seismic events where green symbols are events recorded at both the K and S well (38 events), red circles are events only recorded at the K-well (56 events) and blue circles are only recorded at the S-well (18). Grey circles show $M_w > -1$ events (using contractor estimates). (b) The dotted rectangle outlines seismicity (90 events) linked to stimulation at stage A14, denoted by a black diamond.

use

$$A(f) = \sqrt{S(f) \times T}, \tag{2}$$

where $A(f)$ is the displacement amplitude spectrum and T is the time window used to capture the phase arrival. This leaves us with units of metre seconds.

3.2 Resolution

In this section, we consider the limitations that the instruments and data place on our ability to resolve corner frequencies. It is crucial to delineate the boundaries of the accessible frequency range as this affects the interpretation of results. This was exemplified by Ide & Beroza (2001), who showed that the underestimation of radiated energy in various studies can lead to erroneous interpretations.

To determine the range of resolvable corner frequencies, we first calculate theoretical seismic moment values using

$$M_o = 10^{\frac{3}{2}M_w + 9.1}, \tag{3}$$

from Hanks & Kanamori (1979), where M_o is seismic moment and M_w is moment magnitude. Using these seismic moment values, we then determine hypothetical measurements of corner frequency assuming constant stress drops for the purpose of this section only using Brune (1970):

$$\Delta\sigma = \frac{7}{16} M_o \left(\frac{f_c}{\kappa\beta}\right)^3, \tag{4}$$

where corner frequency is f_c, κ is a constant related to the model used and β is shear wave velocity. We assume $\kappa = 0.32$ (see Section 4) and $\beta = 3800$ m s^{-1}.

For a range of hypothetical M_o values, we calculate the corresponding f_c for four different stress drops (Fig. 3). We determine the lowest $M_{w,c}$ event for which a corner frequency can theoretically be recorded with a 1 MPa stress drop by plotting a vertical line, intersecting at $M_{w,c} = -2.7$ (Fig. 3). The lower frequency detection limit is plotted at 15 Hz (the natural frequency) and the upper limit at 2000 Hz (the Nyquist frequency).

Next we determine the range of maximum corner frequencies based on the percentage of radiated energy captured. We use the following equation (Ide & Beroza 2001)

$$F(f, f_c) = \frac{(-f/f_c)}{(1 + \frac{f}{f_c})^2} + \tan^{-1}(f/f_c), \tag{5}$$

where F is the percentage of radiated energy captured, a function of the sampling frequency f and the corner frequency f_c. We set an upper limit to f_c of 500 Hz, where at least 75 per cent of the radiated energy is captured. The bandwidth limitation has a more severe

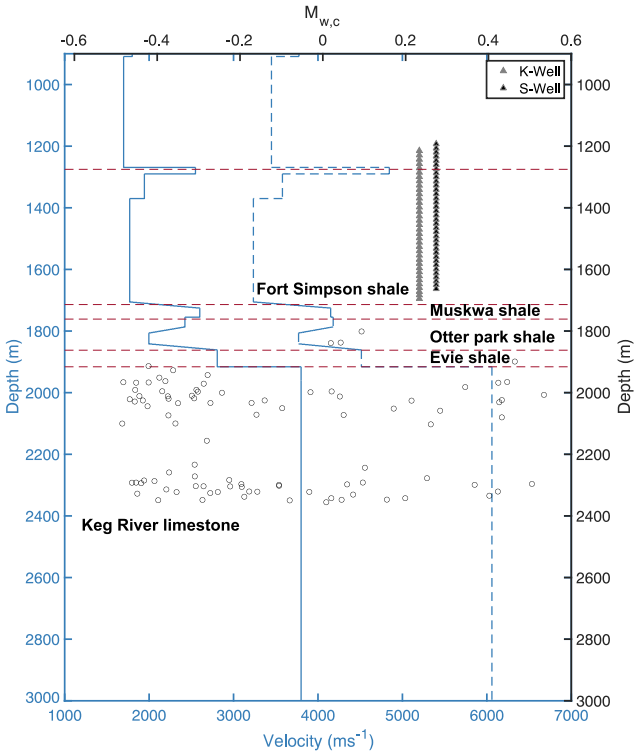

Figure 2. Tapered velocity model with geological formations. Black circles denote depths and moment magnitudes of events calculated by the contractor ($M_{w,c}$) that meet processing criteria. Grey and black triangles indicate geophones in the K- and S-well, respectively. Solid blue and dashed blue lines show *S*- and *P*-wave velocity profiles, respectively.

effect on estimates of apparent stress, based on radiated energy, but can also affect the maximum corner frequency.

We further investigate the resolution of corner frequencies by considering the acceleration spectra. Ideally, we would expect the shape of the acceleration spectrum to show one point of curvature change, corresponding to the f_c, followed by a plateau to higher frequencies. If such an idealised spectrum is attainable, it would yield the most robust fit to a Brune model.

Within this data set only the *P*-phase arrivals at the K-well show a plateau (Fig. 4), whereas most *S* phases do not. Along both wells, we also observe a systematic cut-off of the high-frequency acceleration spectrum, occurring at ∼400–500 Hz along the K-well and ∼200–300 Hz along the S-well. Such an abrupt cut-off might be explained by f_{max} (Hanks 1982; Anderson 1986). Because we are unable to observe a flat plateau for *S*-phase acceleration spectra, it is impossible to know if we are observing the first corner frequency (i.e., f_c) or a cut-off frequency. For this reason, we exclude the S-well from determining source parameters in Section 5.5 and only use *P*-phase arrivals at the K-well.

We then impose 2 additional criteria based on observations during processing. We only use events that show accurate picks on the primary arrivals across all stations using the STA/LTA picking method. The lowest $M_{w,c}$ event that meets this requirement is a $M_{w,c} = -1.2$ event (Fig. 3). We also require that all signals should record a SNR > 3 at 500 Hz, to ensure enough of the high frequency is sampled. We find the lowest $M_{w,c}$ event that meets this requirement is a $M_{w,c} = -0.8$ event (Fig. 3). This leaves us with a $-0.8 < M_{w,c} < 0.55$ range for our spectral analysis, for which we find a total of 112 events. 38 events are recorded at both wells, 56 at the K-well only and 18 events at the S-well only (Fig. 1).

4 METHODS

4.1 Modelling individual spectra

Most studies that calculate source parameters through model fitting procedures use the Brune (1970) model. Madariaga (1976) expanded on this model by approximating a dynamic rupture where the fault plane is modelled as a circular crack. Using this analytical solution, we can determine source properties using (Brune 1970):

$$u(f) = \frac{\Omega_o e^{\frac{-\pi f t}{Q}}}{[1 + (\frac{f}{f_c})^2]}, \tag{6}$$

where u is the far-field displacement spectrum, Ω_o denotes the amplitude of the low-frequency plateau, t is the traveltime of the dominant phase arrival, f is frequency and f_c is corner frequency. There is also an attenuation term, Q, where $1/Q$ represents the loss of energy per cycle.

We must estimate four unknowns: Q, t, f_c and Ω_o. When determining source parameters in Section 5.5, we fix Q and Ω_o to constants. We determine Ω_o from the low frequency amplitude and Q using the whole path attenuation, as explained in Sections 4.3 and 5.4. Traveltime t is also constrained, as explained in Section 2. We then optimize the fit of eq. (6) to single station displacement spectra using @fminsrchbnd in MATLAB to obtain corner frequencies.

To determine f_c uncertainty, we bootstrap the residuals between the model fit and observed data. We calculate the residuals at each frequency point in log space and then resample 30 times and add these residuals to the original spectrum to create 30 new synthetic spectra. We then invert each of these synthetic spectra to calculate 30 new f_c estimates that provide a measure of the variance of each station estimate.

The initial f_c estimates must lie within the range of f_c from inversion of the synthetic spectra and must not saturate at the bounds (15–2000 Hz). We also calculate the root mean square (RMS) at each station and inspect which stations show the best fits based on the RMS.

Once the corner frequency is determined, it can be related to the rupture radius, using (Madariaga 1976):

$$r = \frac{\kappa \beta}{f_c}, \tag{7}$$

where f_c is the corner frequency, κ is a constant related to the radiation pattern, β is shear wave velocity and r is source radius. Madariaga (1976) showed that we expect the f_c to vary with azimuth around the focal sphere relative to the nodal plane of an event by as much as a factor of ∼1.7 for *P* waves and up to ∼2.5 for *S* waves. κ averages this effect out by assigning κ as 0.32 for *P* waves and 0.21 for *S* waves. In the Brune model κ is derived from a simpler kinematic method and is around a factor of 2 larger than in the Madariaga model (Madariaga 1976).

Using corner frequency estimates obtained by model fitting, we can use the Eshelby (1957) equation for calculating stress drops from a circular fault in an elastic half space using:

$$\Delta\sigma = \frac{7M_o}{16r^3}, \tag{8}$$

where M_o is the seismic moment that we estimate in Section 4.2 and r is the rupture radius from eq. (7).

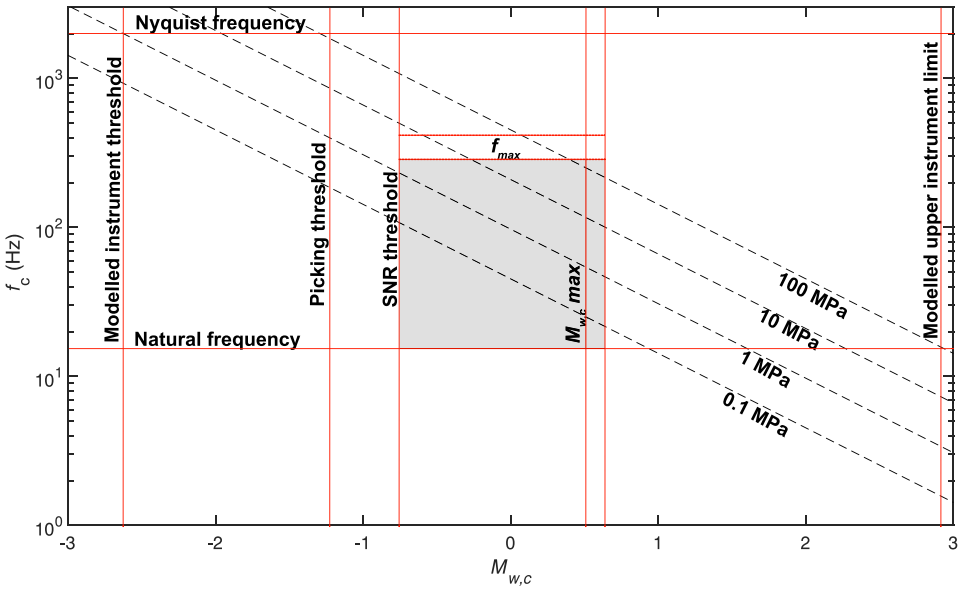

Figure 3. Theoretical f_c against $M_{w,c}$ with red lines showing the multiple constraints from data and instruments that limit the range of magnitudes and corner frequencies that are resolvable (grey rectangle). Dashed black lines show the scaling relationship between corner frequency and $M_{w,c}$, assuming a range of constant stress drops and self-similar scaling using a Madariaga (1976) model. To construct the stress drop lines, we assume $\beta = 3800$ ms^{-1}, from the *S*-wave velocity in the Keg-River formation, where most of our events are located.

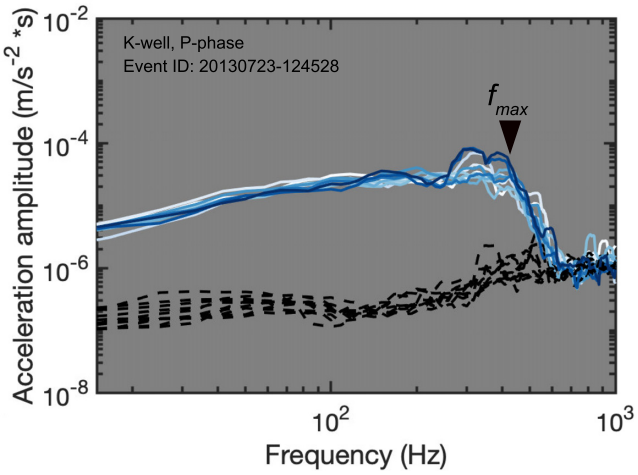

Figure 4. Acceleration spectra from the *P*-phase component of a $M_w = 0.1$ event recorded at the K-well. The solid lines are the observed signals using a 0.1 s time window, and are colour coded according to station depth: darker blue indicates a deeper station. The dashed black lines represent the spectra of pre-event noise.

To calculate stress drops, we first determine the mean corner frequency of each event by averaging the initial f_c estimates over all stations, for a given event; therefore the mean f_c captures the station-station variability. The f_c uncertainty is then calculated by taking 1 standard deviation of the bootstrapped and initial estimates over all stations for a given event. We then calculate the stress drop using eq. (4), and calculate the uncertainty for each measurement using standard error propagation (e.g., Fornasini 2008) of the corner frequency. We only use estimates of stress drop where the standard deviation is less than the stress drop value. To calculate the uncertainty of the average stress drop for all events we combine the standard error from the stress drop distribution and the uncertainty from individual stress drop measurements.

4.2 M_w calculation

To verify contractor provided M_w estimates, we recalculate M_w and compare estimates from this study to the contractor's. We calculate seismic moment using (Brune 1970):

$$M_o = \frac{\Omega_o 4\pi\rho v^3 r}{R_o}, \tag{9}$$

where Ω_o is the low frequency displacement–amplitude plateau, which is determined empirically by taking the mean signal of the displacement amplitude spectra between 20 and 40 Hz. ρ is density, r is the station to event geometric distance, R_o is the average radiation coefficient (0.52 for *P*-phases and 0.63 for *S*-phases) and v is the seismic velocity of the source rock. We use $\rho = 2500$ kg m^{-3} for the Keg-River limestone and a density of $\rho = 2600$ kg m^{-3} for the overlying shale formation, which are determined from sonic logs (Sayers *et al.* 2015).

For each seismic event, we calculate individual station magnitude estimates using *P* and *S* phases by re-arranging eq. (3). Then we average the station M_w estimates to get the event estimate. We measure the uncertainty in this estimate using the standard deviation across station estimates to measure the M_w uncertainty for a given event.

4.3 Modelling attenuation

To constrain an attenuation model we assume that intrinsic attenuation is the dominant mechanism (e.g., Abercrombie 1998). In doing so, we reduce the number of free parameters in eq. (6) by determining Q, decreasing the non-uniqueness of f_c estimations. To model intrinsic attenuation we use (Abercrombie 1997; Bethmann *et al.* 2012)

$$A(f) = A_o(f)e^{\frac{-\pi f t}{Q(f)}}, \tag{10}$$

where $A(f)$ is the displacement amplitude spectrum at a station some distance from the source, A_o is the displacement amplitude at the

source, or some distance closer to A, f is frequency and t is traveltime between the locations where A_o and A are measured. Q as a function of frequency can be expressed as

$$Q(f) = \frac{-\pi f(t_1 - t_2)}{\ln(\frac{A_1(f)}{A_2(f)})}, \quad (11)$$

where $A_1(f)$ corresponds to the amplitude spectra at the top five stations, $A_2(f)$ corresponds to the amplitude at the bottom five stations and $t_1 - t_2$ is the traveltime difference between a station pair. If the right-hand side of eq. (11) is a constant, this implies that $Q(f) = Q$ and frequency independent Q is a reasonable approximation.

We use two methods to determine Q. In the first method, we calculate the attenuation of the wavefield in the rock volume between the top five and bottom five stations. For each event, we calculate spectral ratios between five station pairs that are separated by the maximum possible distance (i.e., stations 1 and 30, 2 and 31, etc.). For each event we stack the signal obtained from all the station pairs to obtain an empirical path term. We then calculate $Q(f)$ using eq. (11). This method provides an estimate of the attenuation within the layer in which the geophones are situated (e.g., Abercrombie 1998; Bethmann *et al.* 2012) but does not necessarily characterize the crustal attenuation of the underlying lithological units along the ray path.

To address this, we also estimate a whole path Q using idealized source spectra over 3 stress drops (1, 10 and 100 MPa), which represent the empirical range across stress drop studies (Abercrombie 1995, 2021). Similar methods have been used to validate Q estimates by Ide *et al.* (2003) and Imanishi *et al.* (2004). To calculate idealized source spectra we determine corner frequencies which correspond to 1, 10 and 100 MPa stress drops. We calculate our own estimates of seismic moment in Section 5.1. Then we use eq. (6) to calculate the expected source spectra. To ensure the signal from the source model is larger than the observed spectrum, we fix the low frequency plateau of the idealized source spectra to 1.1 times the observed Ω_o. When using this method there are unexpected and unrealistic effects on $Q(f)$ below 100 Hz, which are most likely caused by a slow hump in the spectral amplitude observed between 30 and 100 Hz (see Fig. 12). Therefore to avoid potential artefacts in $Q(f)$ we limit our analysis to frequencies above 100 Hz.

For each station we deconvolve the observed instrument corrected spectrum with the corresponding source model to obtain source corrected spectra (i.e., the path/site term) using 1, 10 and 100 MPa stress drops. We then stack spectral ratios across events at each station. This leaves us with 35 spectral ratios corresponding to each station along the borehole geophone array. Then we determine $Q(f)$ at each station using eq. (11).

5 RESULTS

5.1 M_w calculation

In this section we calculate M_w to provide a comparison to contractor estimates. Where possible, we include seismic data from both wells, and use information from P and S phases. On average, we use 94 phase arrivals for each M_w estimate, across both wells. We calculate individual station M_w estimates and event estimates. Below $M_{w,c} = 0$, most of our estimates lie within one standard deviation of contractor estimates apart from 5 outliers (Fig. 5a). Above $M_{w,c} = 0$, we find more discrepancy. 16 estimates of our M_w are more than one standard deviation different to contractor estimates (Fig. 5a).

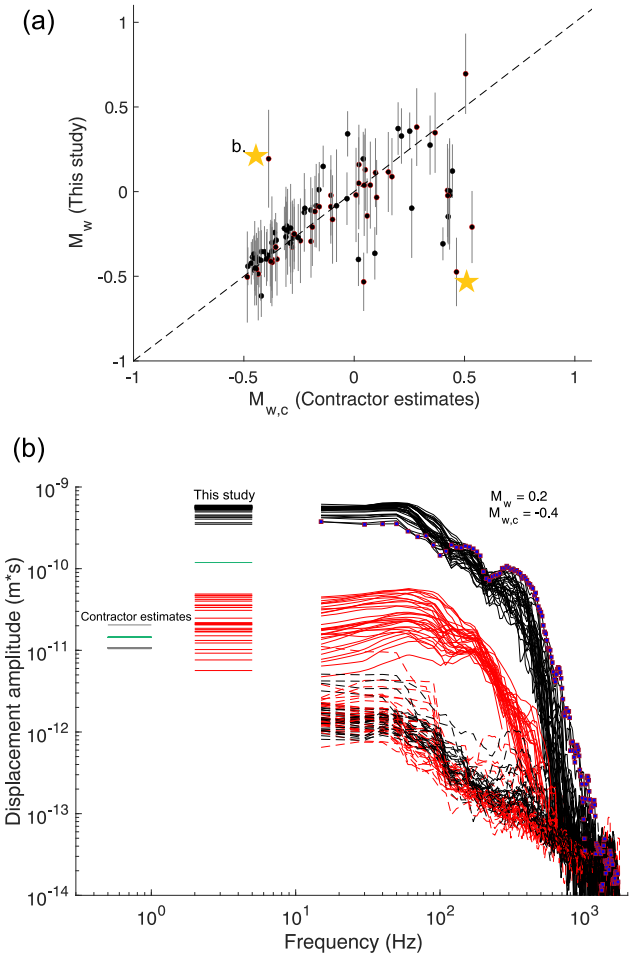

Figure 5. Comparison of our moment magnitudes with those of the contractor. (a) Event and station M_w estimates of 94 events considered for source parameter estimation in Section 5.5 using P and S phases. (a) Average magnitudes (circles) with $\pm 1\sigma$ standard deviation (grey error bars) for events recorded by one borehole array (black circles) and both borehole arrays (black circles with red edge colour). Yellow stars highlight the largest deviations (b) Displacement amplitude spectra (P-phase) of signal and noise from all stations for an outlier event, demonstrating an underestimate of contractor estimates compared to estimates in this study. Thin red and black solid lines are spectra from the S- and K-well, respectively. Thick horizontal lines indicate Ω_o estimates of spectra with the same colour. Blue squares show frequency sampling space (10 Hz). Grey horizontal lines show implied contractor Ω_o. Green horizontal lines show median Ω_o estimates.

To investigate the discrepancy in M_w estimates, we analyse the displacement amplitude spectra (Fig. 5b) from the $M_w = 0.2$ outlier event, which shows the largest underestimate by the contractor and the $M_w = 0.45$ event, corresponding to the largest overestimate by the contractor (Fig. 5a). The largest contractor underestimate is shown in Fig. 5(b). Assuming the contractor uses the same values of r, V_p and ρ, contractor estimates of Ω_o appear to correspond to the S-well spectra only (Fig. 5b). The S-well shows lower spectral amplitudes than the K-well across the frequency range for many events, which is most likely caused by the greater distances that the seismic wavefield has travelled compared to the K-well.

To match the largest contractor underestimate of 0.6 M_w units (i.e., 8 times more seismic moment in our estimate), either r or ρ need to be a factor of 8 smaller. As we consider the shortest possible path from event to station it is not possible for r to decrease. If ρ is

Table 1. Noise features. The K- and S-well columns show which stations show the feature strongest. The CMP lists the components where the feature is strongest. A dash indicates the feature is not seen. 'var' indicates that the feature is not clearly systematic to certain stations and n/a means that the strongest component is not obvious.

Feature	Frequency (Hz)	K-well stns	S-Well stns	CMP
NF1	450–600	1–10	–	N/Z
NF2	250–400	27–35	var	n/a
NF3	550–650	–	20–35	n/a
NF4	50–80	–	All	n/a

a factor of 8 smaller, it would be unrealistically small (i.e., $\rho = 310$ kg m^{-3}) compared to a density of ∼2500 kg m^{-3} expected from the Keg-River limestone (Sayers *et al.* 2015).

For contractor overestimates, the largest discrepancy is 0.9 M_w units (i.e., a factor of 22 times more seismic moment in contractor estimates). It is likely that r is slightly larger because we assume a straight line path from source to receiver. However, because density between layers is similar (Sayers *et al.* 2015), it is unlikely that ray paths will be significantly longer than a straight path. If density changes, it would also need to increase by an unreasonably high value (i.e., 55 000 kg m^{-3}) to explain the difference.

Thus, single parameter changes do not explain the M_w outliers from this study compared to the contractor. Methodological differences may explain the discrepancy between our estimates and contractor estimates but the contractor's methods are not provided. For the purpose of this study we use our own estimates of M_w.

5.2 Spectral features of noise

In this section, we analyse features of the noise spectra to better understand the instrument response, as are summarized in Table 1. We start by analysing spectograms of seismic events in NEZ orientation and then analyse the pre-event noise along both wells. At most stations we observe unexpected peaks in the noise spectra that are continuous.

We select ∼4 min of seismic data from consecutive event-separated SAC files in 'stitched events' and identify systematic features in the spectograms. Along both wells, peaks are strongest in the *Z*-component, though observable across all components. At the K-well, the shallowest stations (i.e., stations 1–10) shows a peak at ∼400–600 Hz (Fig. 6a). Towards deeper stations, the peak migrates to a lower frequency band at ∼250–400 Hz (Fig. 6b). At the S-well, all stations show a clear peak at 50–80 Hz (Fig. 6c and d). At the shallowest station, we observe peaks at ∼300–400 Hz (Fig. 6c). Towards the deeper stations, we observe a faint higher frequency band peak at ∼500–700 Hz (Fig. 6d).

Next, we analyse the pre-event noise from the far-field displacement of all 112 events on NEZ components using a 0.1 second time window (Fig. 7). Most stations show amplification features that usually appear as notches. Along the K-well the pre-event noise shows high frequency noise amplifications that are strongest on the *Z* and *N* components. The two clearest resonance features are highlighted in Figs 7(a), (c) and (e) at ∼450–600 Hz (Noise Feature 1) and ∼250–400 Hz (Noise Feature 2). Noise Feature 1 (NF1) appears to be systematically stronger at shallower stations (i.e., stations 1–10) while Noise Feature 2 (NF2) appears to be systematically stronger at deeper stations (i.e., stations 27–35). However, there is still variation from station to station (e.g., station 35 does not show a particularly strong level of NF2).

Along the S-well the clearest feature is a notch at ∼550–650 Hz which appears strongest at the deeper stations (i.e., 20–35). We also observe a clear sharp increase in the spectra below 100 Hz, which may correspond to the strong peak seen in the stitched event spectograms at 50–80 Hz (Fig. 6).

5.3 Station limitations

Next we investigate the limitations on retrieving source parameters based on station position in the borehole geophone array. While getting closer to the seismic source should enable us to retrieve high frequency information, and better constrain earthquake source models, we find that deeper stations are systematically more compromised in retrieving high frequency information along both borehole geophone arrays.

To visualize the issue, we normalise *P* and SH spectra to the first Fourier coefficient of the signal using the shallowest (i.e., station 1) and deepest station (i.e., station 35). We then also normalise the noise to the first Fourier coefficient of the signal such that the point of intersection between signal and noise corresponds to SNR = 1 in Fig. 8.

To guide the eye we determine theoretical model curves using $Q = 170$, and determine traveltimes to stations by fixing the *S*-wave speed to 3800 ms^{-1} and adjust the distance travelled to the best visual fit. The aim here is not to provide constraints on the attenuation model but rather to display the shape of the expected spectrum against the observations at stations 1 and 35.

At station 35, the *P*-phase clearly shows a severe loss of high frequencies above approximately 400 Hz, which is likely associated with f_{max} (Fig. 8a). As a result, high frequencies deviate significantly from the expected Brune spectral shape, preventing an acceptable model fit to the data. We find that a κ modified model (Ktenidou *et al.* 2014) does not visually improve the fit. The theoretical curve for Station 1 shows a significantly better explanation of data between around 100–500 Hz, but underestimates the low frequencies (i.e., 30–100 Hz).

From observing the SH-phase spectra in Fig. 8(b), the *P*-wave coda causes resonances in the SH phase arrival, which is especially notable in the deepest stations. The shallower stations on the shear wave components show the cleanest spectra, but have a relatively small bandwidth of good SNR. For this reason we exclude shear waves from further analysis and only consider *P*-phase arrivals at the K-well when determining source parameters in Section 5.5. As we exclude the S-well, we are now left with 94 events.

We further constrain which stations and phase arrival we can use for estimating stress drops. The deepest stations (i.e., stations 15–35) along both wells have a high frequency fall-off that is severely affected by f_{max}. This is demonstrated for station 35 in Fig. 8(a), as annotated. Therefore we also limit our analysis to stations 1–15 when determining source parameters in Section 5.5.

To further investigate the nature of the resonances we select a cluster of seismic events colocated within 100 m of a reference event (i.e., 'target event') and highly cross correlated between 60 and 300 Hz with the chosen target event. If two colocated events are highly cross correlated (i.e., CC > 0.9), we should be able to assume that the path and site effects recorded at a single station should be approximately the same, and that any variation should come from the source term. Fig. 9 shows significant variation in the expression of resonances from a cluster of seismic events co-located and highly cross-correlated with a target event, when spectra are normalised to the lower frequency plateau (15–40 Hz). In some cases there is a

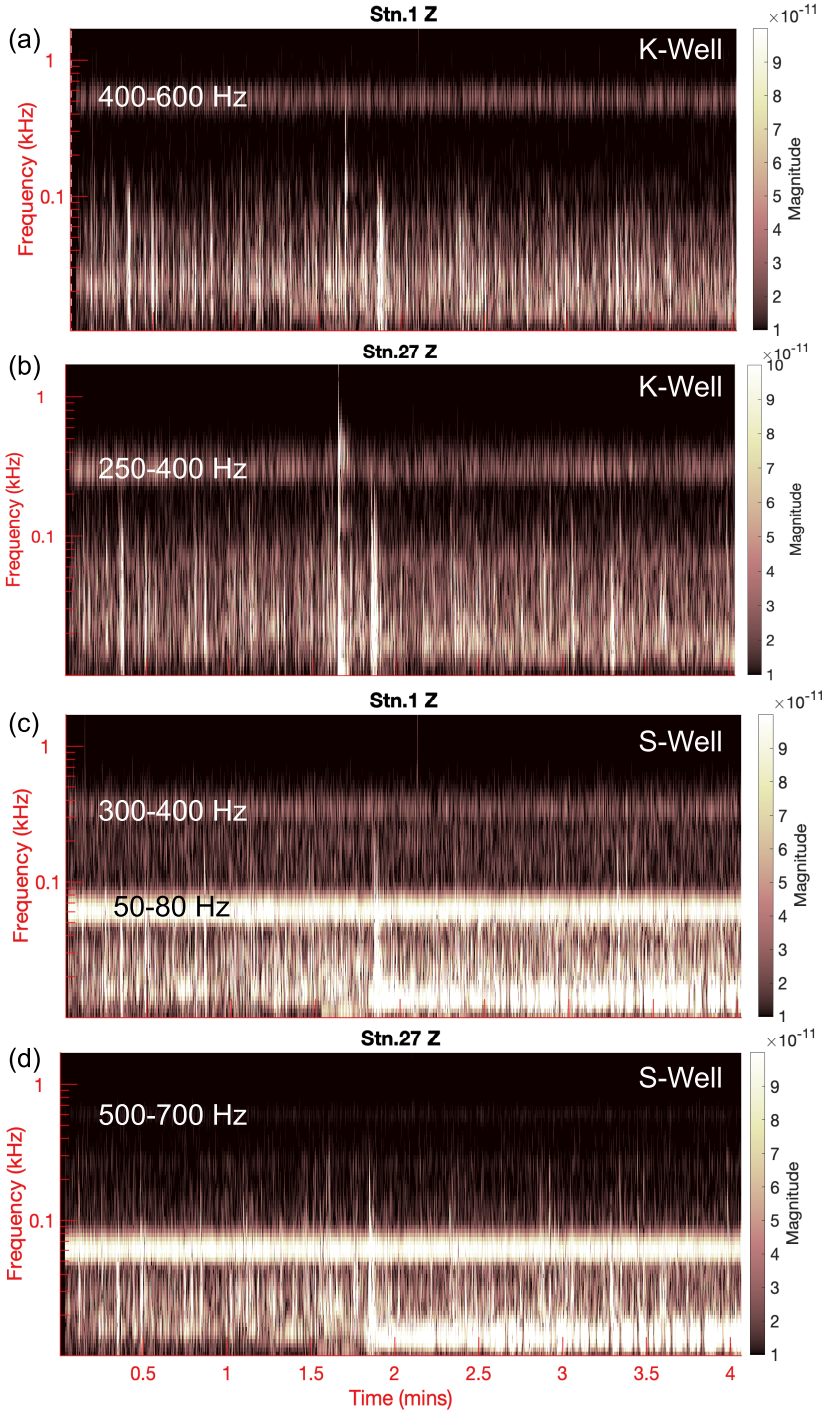

Figure 6. Continuous wavelet transforms of ∼4 min of stitched seismic events, showcasing salient noise peaks in the *Z*-component at (a) K-well, station 1, (b) K-well, station 27, (c) S-well, station 1 and (d) S-well, station 27.

factor of ∼10 difference in the relative amplitude between events. These resonances are unlikely to result from source term variations. Instead, they suggest a sensitivity to small differences in path or variable site effects. This sensitivity will persist into spectral ratios and may thus compromise the validity of the approach. Stacking the EGFs may improve the stability of the spectral ratios and is likely a better approach, but resonances may still not be completely removed.

5.4 Modelling crustal attenuation (Q)

We consider two methods of determining Q from *P*-phase arrivals using events recorded at the K-well. For both methods we consider the possibility of frequency independent and frequency dependent attenuation. Our analysis suggests that a frequency independent model provides agreement with observed data. For the purposes of calculating Q using Method 1 we restrict our analysis to events that occur below the shale formation such that spectral ratios between

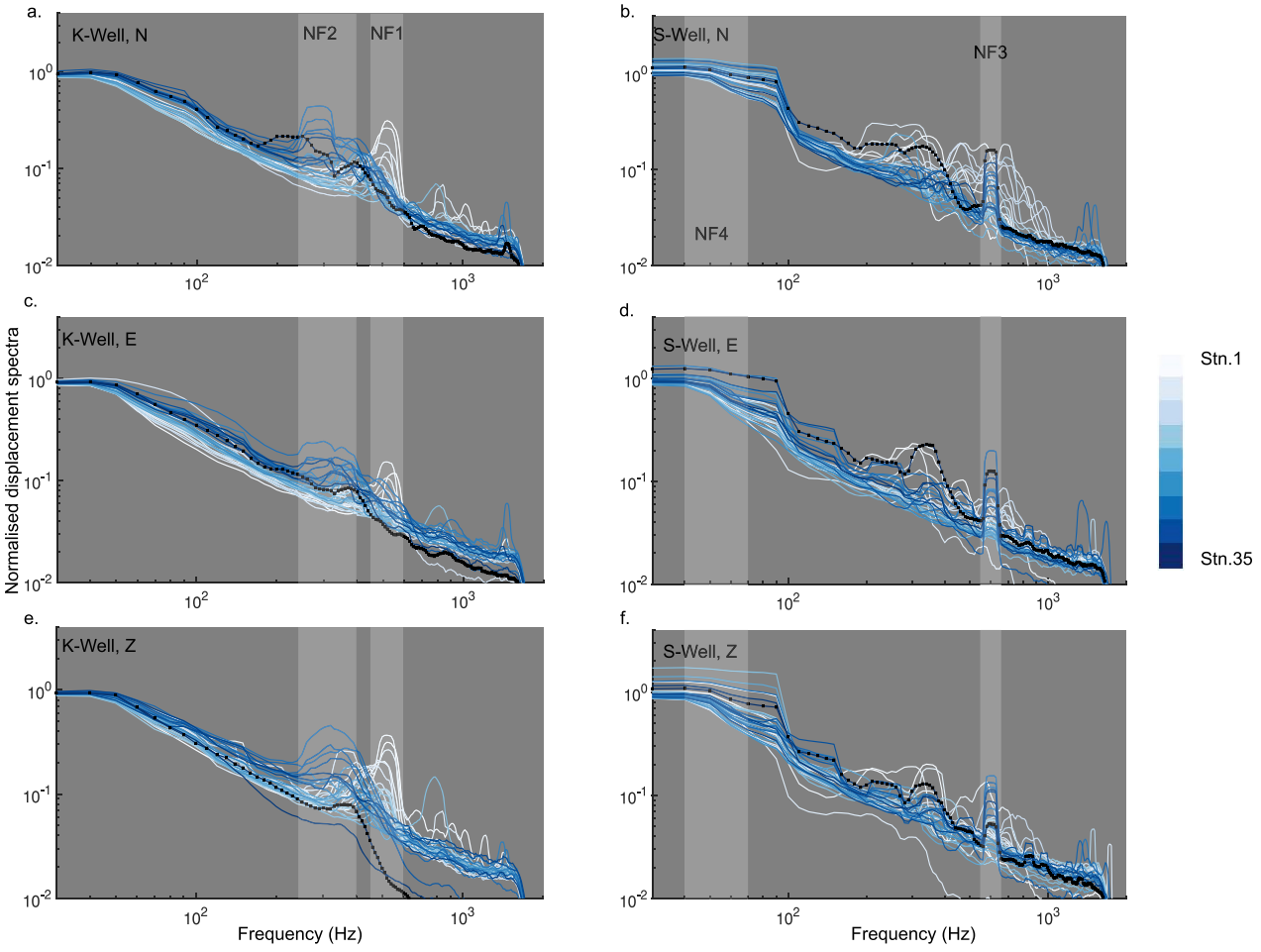

Figure 7. Systematic resonances in pre-event noise using 112 events from the (a, c and e) K- and (b, d and f) S-well. Each line represents the stacked pre-event noise spectra across events and are colour coded according to station depth where darker blue indicates a deeper station along the borehole array. Noise Features (NF) are highlighted with patches and are annotated according to Table 1. Black squares show frequency sampling points for the deepest station (i.e., station 35).

stations correspond to a clear difference in traveltime (86 out of the 94 events); for Method 2 we use all 94 events.

5.4.1 *Method 1*

Our ability to resolve attenuation using Method 1 is limited by the maximum distance between stations along the borehole array. The low frequency amplitudes of the deepest stations are smaller than the shallowest stations at the K-well, which might be caused by a radiation pattern effect. Relatively high frequencies are enriched at deeper stations because the effect of attenuation dominates. As a result, the deepest station only shows a clearly larger amplitude at or above ∼180 Hz (Fig. 10a). Therefore, we restrict our analysis to 26 out of the 86 events where the spectral ratio between the deep and shallow stations is >1 at 180 Hz (Fig. 10a). By limiting our frequency range to above 180 Hz we are using spectral information above the apparent corner frequencies observed at most stations, but it is our best lower frequency limit, as shown in Fig. 10(b). On average, above 180 Hz, we obtain a Q estimate of 160 ± 50 using Method 1. The large uncertainty (± 50 using 1σ) reflects the bumps in the spectra.

5.4.2 *Method 2*

To avoid the effect of resonances, we limit our analysis to the top five stations of the K-well array for Method 2. Between 100 and 280 Hz, the stacked spectral ratios from stations 1–5 show a relatively straight line in log-linear space (i.e., constant Q), as shown in Fig. 11. Above 280 Hz, resonances introduce scatter into Q measurements, which is especially notable at station 3 (Figs 11b, d and f). Q uncertainty increases towards lower stress drops because resonances are relatively larger when the spectral ratio is calculated in the high frequency decay portion of the source spectrum relative to the low frequency plateau for higher stress drops. We also observe a systematically higher Q for lower stress drops because less attenuation is needed to explain the reduction in amplitude. For each stress drop model, we calculate an average Q across all stations as $Q = 180 \pm 40$, $Q = 120 \pm 20$ and $Q = 110 \pm 20$ for a 1, 10 and 100 MPa source model, respectively.

5.4.3 *Comparison of Q methods*

Both methods show that a frequency independent attenuation model is broadly consistent with observed data above 180 Hz for Method 1 and 100 Hz for Method 2. The larger uncertainty associated with

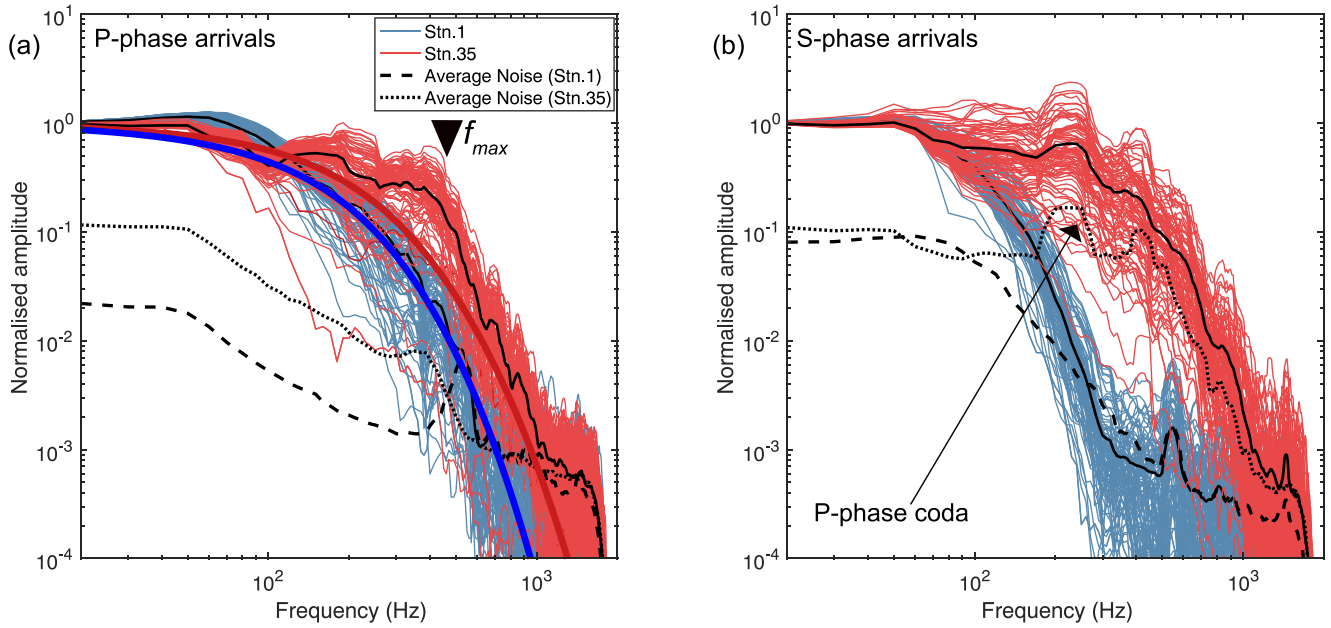

Figure 8. Normalised spectral amplitude of station 1 and 35 across all events along the K-well, with annotations pointing out limiting effects on deeper stations. Solid black lines represent the mean signal for station 1. Thick red and blue curves in (a) represent theoretical source models for *P*-phase arrivals at station 35 and station 1, respectively. (b) Lines correspond to same description as (a) for the SH-phase arrival.

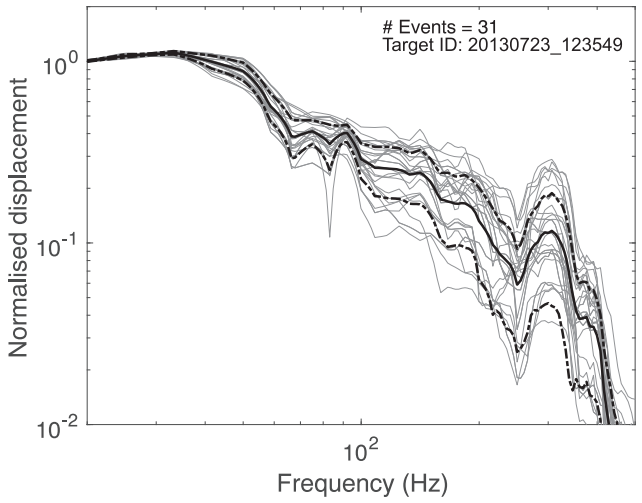

Figure 9. Normalised displacement-amplitude spectra of the *P*-phase arrival from a cluster of co-located microseismic events recorded at station 9. Grey solid lines show normalised displacement amplitude spectra. Black solid line shows average signal and dashed lines show $\pm 1\sigma$ at each frequency point. We found 31 nearly colocated events within 100 m and high cross correlation (i.e., CC $>$ 0.9) of the target event.

Method 1 means that Q is not statistically different relative to any of the Q estimates using Method 2. For this reason, we only consider the three estimates from Method 2.

To assess how well the Q values explain the observed spectra, we apply Q corrections to 1, 10 and 100 MPa source models (Fig. 12). Between 30 and 80 Hz, modelled spectra are smaller than the data. From 100 to 400 Hz the models explain the data relatively well. Above 400 Hz, we see bumps in the spectra, which causes an underestimate by the model. For determining corner frequencies in Section 5.5, we consider all three values of Q from Method 2.

Although a frequency independent Q appears to provide a decent explanation of the data, the resonances might mask a frequency dependence which may be more obvious at deeper stations. However, the deeper stations are compromised by stronger resonances, and are therefore not included in the Q calculation.

Importantly, corner frequency visually appears to be relatively stable across the range of 1.1 magnitude units (Fig. 12), although quantitative estimates are needed in case the differences emerge given different distances of the path. Nonetheless, because of the relatively small M_w range we are unlikely to resolve significant differences in apparent corner frequency. Additionally, the percentage of energy removed becomes exponentially larger at higher frequencies, which also causes a relatively stable apparent corner frequency.

5.5 Corner frequency and stress drop estimation

As discussed in Sections 3.2, 5.2 and 5.3 the bandwidth limitations, f_{max} effects and high frequency resonances compromise the robustness of source parameter estimates. Notwithstanding these limitations, we carefully attempt corner frequency and stress drop estimations. We determine f_c for each station using the method outlined in Section 4 for three different Q estimates, as explained in Section 5.4. Then we calculate event estimates of f_c to compute stress drops. To test the hypothesis that injection pressure affects stress drop, we select events at a period where we might identify a trend from the injection point to the bottom of the fracture zone. Therefore we limit our analysis to events associated with injection of stage A14 (i.e., 90 out of the 94 events at the K-well).

By analysing the distribution of stress drops from three crustal attenuation models, we disqualify models that provide unrealistic stress drop values (e.g., $>$ 400 MPa) and those that generate a broad range (e.g., $>$ 100 MPa), as shown in Fig. S1. Based on these criteria, $Q = 110$ and $Q = 120$ provide stress drop estimates that are physically unrealistic (i.e., $>$ 500 MPa). Such high estimates are unlikely for strike-slip faults in the upper crust, given that shear

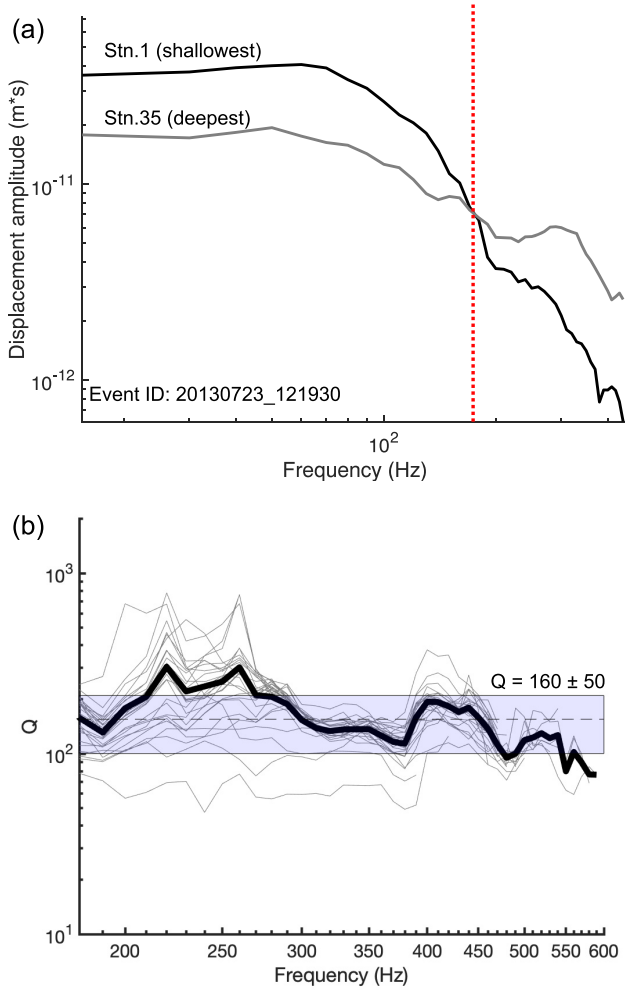

Figure 10. Determination of frequency independent Q using station pairs along the geophone array (Method 1) at the K-well. (a) An example of a station pair showing displacement amplitude spectra of *P*-phase arrivals. Dotted red line is the limit above which signal from the deeper station is larger than shallower station. (b) Q against frequency for all 26 events we consider for Q estimation using Method 1. Each grey line represents the stacked signal across five station pairs. The thick black line shows the average signal over all the stacks for all events. Dashed black line shows average Q estimate and blue patch shows uncertainty corresponding to $\pm 1\,\sigma$ standard deviation.

strength is not expected to exceed ∼20 MPa (Streit 1997). $Q = 180$ provides the most physically reasonable estimates of stress drop between 0.1 and 9 MPa. For this reason, we only consider the $Q = 180$ model further. This Q value falls within the uncertainty of $Q = 226 \pm \sim 70$ calculated by Yu *et al.* (2020) for seismic events recorded in the crystalline basement at a hydraulic fracturing pad 240 km away from this study, which adds further credibility to our estimate.

Considering that there are some systematic differences between source and model, as mentioned in Section 5.4, we only use the most robust fits to calculate first order estimates of f_c. From visual inspection, stations with an RMS < 4 show the most robust fits, which we use as an additional criterion. Using all the fitting criterion, fits are decent, as shown in Fig. S2.

Results of corner frequency and stress drop estimates are shown in Fig. 13. We do not know whether the contractor used a Brune or Madariaga model, therefore we show contractor values as a range spanning both. Corner frequency estimates calculated in this study are on average larger than estimates made by the contractor and lie mostly between the 1 and 10 MPa theoretical stress drop lines (Fig. 13a). Along the borehole array, corner frequencies do not systematically depend on geophone depth (inset Fig. 13a). We find a mean corner frequency of 210 Hz ±30, using the standard deviation across our estimates ($\pm 1\sigma$).

Based on observations of a systematic f_{max} at 400–500 Hz along the K-well, corner frequencies are likely underestimated, especially for smaller events, which may explain the shallower gradient of $f_c \propto M_w^{-0.35}$ from the line of best fit compared to what we expect from self-similar scaling ($f_c \propto M_w^{-0.5}$). Note that we use here the moment magnitude instead of seismic moment as the self-similar scaling variable. Therefore our mean corner frequency and stress drops are probably rough estimates of possibly larger values. Corner frequencies below f_{max} should be actual corner frequencies, even if uncertain. Values above f_{max} may represent f_{max} rather than f_c. The lack of estimates near ∼100 Hz is likely a source effect caused by the largest size of seismic events we use, which places a lower limit on the corner frequencies available to analyse. The upper limit of f_{max} can be seen as the cut-off in Fig. 13(a) and scaling in Fig. 13(b).

We calculate an average stress drop of a 1.6 MPa ±1.2 using the geometric mean of the stress drop. Our results are broadly in the expected range of 0.1–100 MPa observed from earthquakes (Abercrombie 1995) assuming self-similarity (Fig. 13b). The scaling of stress drop with M_w that we report in this data set is also seen in the other data sets (Fig. 13b). In our case, the scaling is more likely related to an upper limit of corner frequency resolution than a source effect.

Spatially, there are two populations of events. The shallower population spans the bottom of the stimulated rock volume into the underlying limestone; the deeper population is a few hundred metres deeper in the limestone. Stress drops do not clearly vary systematically between these populations with depth or distance from point of injection (Fig. 14). We also observe no clear differences between events that occur in the stimulated rock volume and the underlying limestone.

6 DISCUSSION

6.1 Origin of the observed amplifications

We observe unexpected high frequency amplifications along the two borehole arrays considered in this study. Resonances are typical in borehole geophone arrays (e.g., Tary *et al.* 2014; Vaezi & Van der Baan 2014; Zhang *et al.* 2018; Yaskevich *et al.* 2019) and must be carefully analysed to determine which stations are appropriate for source parameter estimation. Here, we attempt to qualitatively identify the clear systematic features across both wells, although there is variation from station to station and between events. Understanding the provenance of the resonances may also help advise operators on how to better deploy the geophones.

6.1.1 Noise features (NF1-3)

We identify three high frequency systematic noise features (NF1-3) across both the borehole arrays from ∼4 min of stitched seismic event data. NF1 are resonances at ∼450–600 Hz, NF2 are resonances at ∼250–400 Hz and NF3 is a notch at ∼550–650 Hz. These features are unlikely to be explained by source effects, which are low frequency and not continuous. Tary *et al.* (2014)

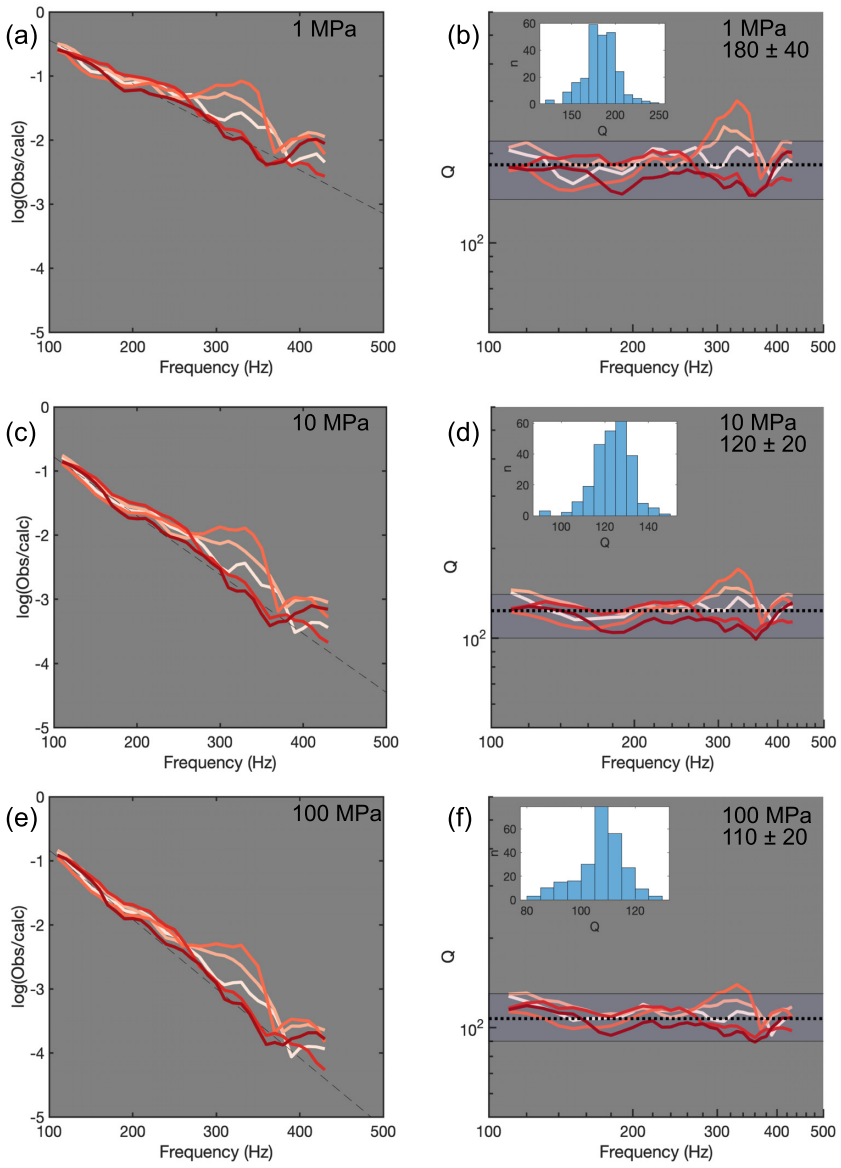

Figure 11. Empirical determination of whole path Q using idealised source spectra assuming 1, 10 and 100 MPa stress drops from 94 events at the K-well (stations 1–5). (a, c and e) coloured solid lines show the stacked spectral ratios between the instrument corrected amplitude and the idealized source spectra against frequency. Black dashed lines shows a linear fit to the deepest station. (b, d and f) Q calculated directly from the spectral ratios as a function of frequency for (b) 1 MPa (d) 10 MPa and (f) 100 MPa source models. Black dotted lines show the average Q with $\pm 1\sigma$ range as a light blue shaded area. Darker red denotes a deeper station in the borehole array. Inset plot shows histograms of Q estimates across different frequencies and stations.

show that fluid-filled fractures from the opening of perforations (∼0.01 m), interconnected fractures and larger cracks (>5 m), resonate between 17 and 31 Hz, which is significantly below the frequency content of NF1-3.

Resonances due to spurious frequencies and self noise are a more plausible explanation of NF1-3, as they can explain both the high frequency nature and the continuous appearance over seismic events. Geophones are prone to off-axis excitation above the spurious frequency limit of 365 Hz and NF1-3 are close to or above the spurious frequency limit. In some cases individual stations show resonances that are below the spurious limit, which is surprising given the instrument specification provided limit of 365 Hz. Spurious frequencies have been recognized as a major challenge for recording accurate phase arrivals (Sleefe *et al.* 1993, 1995; Faber & Maxwell 1997).

The clamping system that locks the geophone in place is another potential source of resonances (Sleefe *et al.* 1993), which is likely to be a continuous feature. The challenge is usually that there are only 2 points of contact between the geophone sonde and the borehole, which can give rise to resonances (Gaiser *et al.* 1988). For this data set, we are not provided with cement bond logs so we must infer how good coupling is from the data. Clamping issues are observed by Gaiser *et al.* (1988), who attribute 130–140 Hz resonances to the coupling of the geophones. A more recent study by Zhang *et al.* (2018) attributes two modes at 120 and 320 Hz to coupling issues. This could explain the presence of NF1-3, even though the resonances in this study are at higher frequencies. It is possible that with more advanced and better instrument setup, resonances are pushed to higher frequencies.

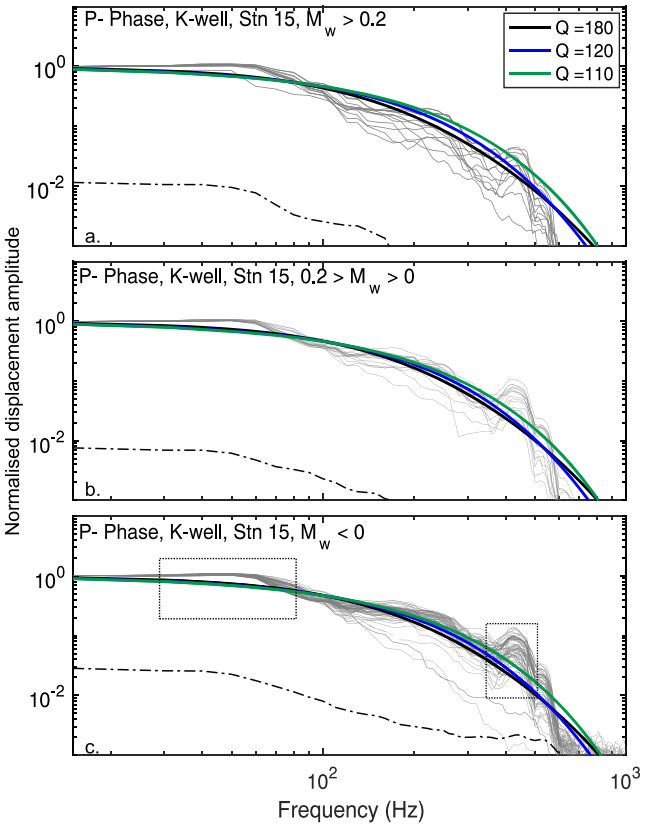

Figure 12. Forward modelled far-field spectra using three candidate models for crustal attenuation compared to observed data based on results from Method 2 of measuring attenuation. Grey thin lines show normalised displacement spectra of the *P*-phase arrival at station 15 from 94 events at the K-well. Spectra are separated into three magnitude bins. (a) $M_w > 0.2$. (b) $0.2 > M_w > 0$. (c) $M_w < 0$. Dashed black boxes highlight deviations from the expected spectral shape. Each curve shows the theoretical model using the average Q estimates from Method 2. Black dot-dashed lines shows average pre-event noise.

6.1.2 *Noise feature 4 (NF4)*

This feature has a lower frequency content of ∼50–80 Hz and appears relatively strong in spectograms, but does not appear in the pre-event spectra. The electrical noise is a likely candidate for the cause, which is expected at around 60 Hz (Tary *et al.* 2014), falling within the range observed. The pumping of fluids may also cause relatively low frequency resonances, however, we are unable to verify this because there is no seismic data before pumping starts.

6.2 Implications of resonances

Most source parameter studies rely on the assumption that the path and site effects of colocated events can be considered the same for analysis at a single station. In this study we find that highly cross correlated, colocated phase arrivals (CC > 0.9) between 60 and 300 Hz show significant variation in the strength of high frequency resonances. This observation can be explained by slight variations in the source, path or site that generate different resonance strengths, which may compromise the spectral ratio approach as resonances are not removed. Stacking the EGFs might provide a more stable signal but may not completely remove resonances.

Resonances introduce significant scatter into empirical measurements of intrinsic attenuation and therefore limit our ability to resolve robust stress drop estimates. When using either method for determining Q, the uncertainty in Q is large (±20–50). Other studies that have measured Q using similar techniques to this study (e.g., Abercrombie 1998) find significantly less uncertainty in Q, although the frequency range of interest is lower (i.e., 1–100 Hz), and resonances are likely less severe.

6.3 Source parameters

6.3.1 *Corner frequencies*

Despite the limitations in retrieving faithful representations of the source spectra, it is still useful to determine corner frequency and stress drops and compare to other regional and global estimates. We calculate 743 initial estimates of *P*-phase Madariaga corner frequencies and 22,380 estimates in total (including synthetic spectra from bootstrapping) with a range of 90–750 Hz and a mean of 210 Hz ± 30 (±1σ). We first discuss the uncertainties in determining f_c and then interpret our results.

One important observation from the spectra is that the apparent corner frequency appears relatively constant over a 1.1 M_w range. This observation can be explained by disproportionately larger attenuation at high frequencies (i.e., > 100 Hz) of the dominant signals we are analysing (Deichmann 2017). Other studies have also highlighted the severe reduction of energy at high frequencies (Eaton *et al.* 2014; Butcher 2018).

Corner frequency resolution is limited by a clear cut-off frequency at ∼400–500 Hz for *P*-phase arrivals the K-well. The cause of the cut-off could be related to f_{max}. Although f_{max} was initially understood as a local site effect from shallow crustal attenuation (Hanks 1982; Anderson & Hough 1984), f_{max} could still apply to borehole geophones. Although one might expect clean signals from borehole geophones, local site effects should not be ruled out (e.g., Ide *et al.* 2003). We should have the bandwidth to measure lower corner frequencies, therefore the lower f_c limit of ∼ 100 Hz is likely a source effect.

It is likely that a low SNR limit and bandwidth limitations are contributing to energy loss and a relatively constant corner frequency. Even though we estimate that at least 75 per cent of the seismic energy is captured, the absence of 25 per cent of high frequencies could contribute to the saturation of f_c in the data set. For microseismic source parameter studies, the underestimation of radiated energy is a commonly observed feature (e.g., McGarr 1999; Ide & Beroza 2001; Ide *et al.* 2003).

Compared to the global study by Allmann & Shearer (2009) of *P*-phase spectra from global tectonic seismicity, f_c estimates in this study lie in the expected range for negative magnitude earthquakes, assuming a constant *S*-wave velocity of 3800 ms^{-1} and a Madariaga (1976) circular crack model. This supports the invariance of stress drop with respect to earthquake size over the large scale. Other studies of microseismic source parameters have also supported self-similarity into negative magnitudes (Hiramatsu *et al.* 2002; Baig *et al.* 2012).

6.3.2 *Stress drops*

We determine Madariaga stress drop estimates from 86 out of the 90 events with a smaller standard deviation than the stress drop estimate itself. The range of event stress drops is 0.2–5 MPa with

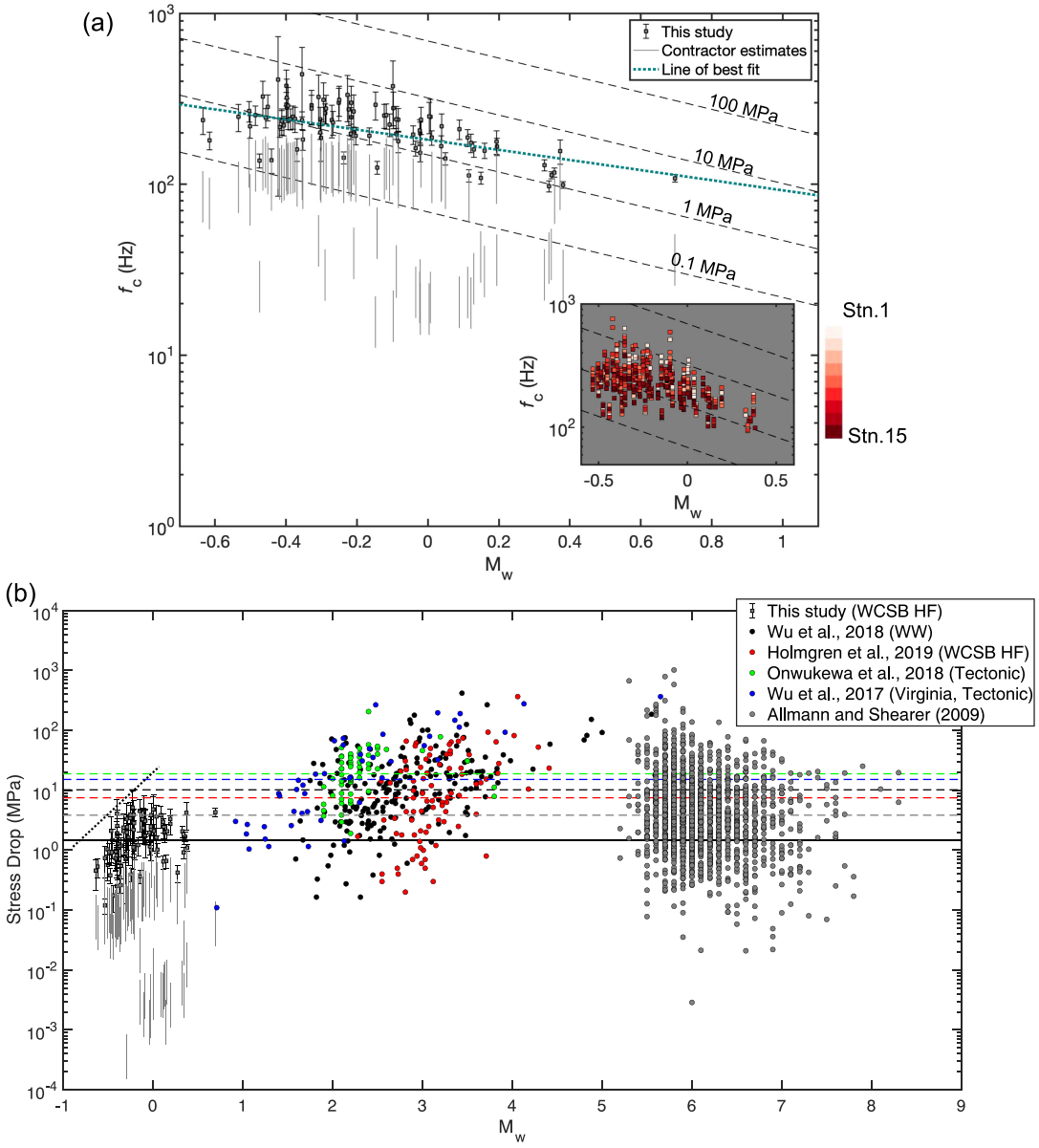

Figure 13. Best available source parameter estimates compared to contractor estimates and source parameter studies from the literature. (a) *P*-phase corner frequency against M_w. Black squares show results from this study and grey vertical lines show contractor estimates over the range corresponding to a Brune and Madariaga source model. Inset shows individual station estimates of corner frequency at the K-well; darker red squares indicate deeper stations. On main and inset plot, theoretical lines of corner frequency against magnitude assume an S-wave velocity of 3800 ms^{-1} and a Madariaga (1976) crack model. (b) Stress drop versus M_w compared to contractor estimates, one hydraulic fracturing (HF) data set, two tectonic data sets, a waste water (WW) induced data set and a global study by Allmann & Shearer (2009). The black horizontal solid line shows the mean estimate of stress drop from this study.

a geometric mean of 1.6 MPa ± 1.2. It is important to keep in mind that the resonances and high frequency cut-offs we observe could be causing some of the trends we observe in regard to stress drop with depth, M_w, and distance from point of injection because high frequencies are preferentially removed. To address this we only calculate results from the shallowest stations (i.e., stations 1–15), where the effects of resonances and high frequency cut-offs are reduced.

Our absolute estimates of stress drop are very similar to the closest and most similar study (at a pad ∼240 km from the pad in this study) by Yu *et al.* (2020). Compared with our estimated mean of 1.6 ± 1.2 MPa, Yu *et al.* (2020) calculate an average stress drop of ∼1 MPa from their best results of proximal seismic events using the spectral ratio method. Proximal events are mostly confined to the sedimentary layer in Yu *et al.* (2020), whereas most events in this study occur in the underlying crystalline formation. The similarity of stress drops (both using a Madariaga constant) between our study and Yu *et al.* (2020) at similar depths and both induced by hydraulic fracturing strongly suggests that the rupture slip to length-scale ratio of seismic events in these two data sets is similar.

We use borehole geophones in comparison to the surface array used by Yu *et al.* (2020). Using a relatively simple fitting procedure we are able to obtain similar stress drops to the values obtained by Yu *et al.* (2020). While it is certainly likely that our absolute estimates are smaller than actual values, because of the effects of high frequency attenuation, it is encouraging to see that

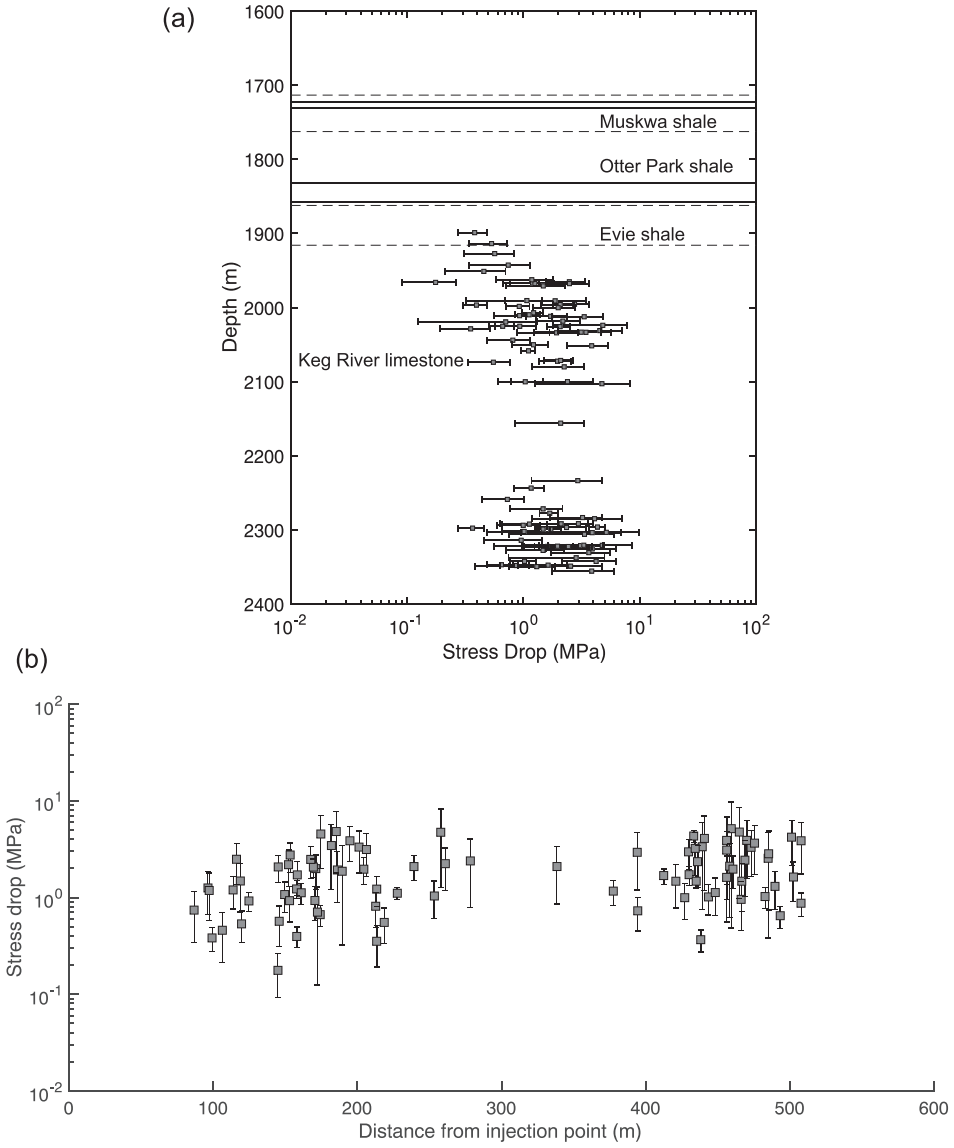

Figure 14. (a) Stress drop against depth and (b) distance from seismic event to injection point.

a borehole array can produce similar results to the closest study, which uses a more sophisticated spectral ratio method. The spectral ratio method practically takes more time compared to directly fitting source models. Thus, this study shows that once a crustal attenuation model is constrained, directly fitting source models from a borehole geophone array may provide decent first order estimates.

Although stress drop estimates in this study are within the expected tectonic range, the average stress drop is below the global average of 4 MPa and lower than the average of 7.5 MPa calculated by Holmgren *et al.* (2019) from an induced seismicity data set in the WCSB. Our average stress drop is also lower than the stress drops between ∼2 and 200 MPa, calculated for a tectonic data set that Onwuemeka *et al.* (2018) calculated in the Eastern Canadian seismic zone. In both these studies some stress drop estimates are greater than 100 MPa, considerably larger than any of the estimates in this study.

Our lower mean stress drop can be explained by several physical causes. First, a lower effective stress may reduce the stress drop (Allmann *et al.* 2011). Secondly, the shallower depth of our events compared to Holmgren *et al.* (2019) and Onwuemeka *et al.* (2018) will result in a lower crustal shear strength which could result in lower stress drops.

The lowest stress drops we might expect for seismic events at the average depth in this study (2.2 km) can be calculated if we assume a relatively simple, but realistic (Moos & Zoback 1990) 2-D Mohr–Coulomb representation of the fault plane, where seismic events are hosted on a strike-slip fault. A strike slip mechanism is expected according to stress gradients recorded from borehole breakouts measurements in the region (Bell 2015) and the world stress map (Heidbach *et al.* 2007). Focal mechanisms studies have also found a dominantly strike-slip mechanism in the region (Wang *et al.* 2018). If we assume the co-efficient of friction along the fault plane is 0.6 and that the fault is critically stressed, we can estimate the shear strength using (Huang *et al.* 2017)

$$S_{ss} = 0.7(\sigma_v - P), \tag{12}$$

where S_{ss} is crustal shear strength, σ_v is vertical stress and P is pore pressure. Assuming a hydrostatic pore pressure of 27 ± 7 MPa and

a vertical stress of 66 ± 6 MPa (Kettlety *et al.* 2019), using stress measurements at depth by Bell (2015), we calculate an available crustal shear strength of 39 MPa ± 9. Based on empirical observations of stress drops from faults in the north and central United States by Huang *et al.* (2017), we expect a minimum of ∼5 per cent of the shear stress to be released (Huang *et al.* 2017), which results in a minimum stress drop of 1.4 MPa ± 0.5. Therefore the average stress drop (1.6 ± 1.2 MPa) we determine at the depth of the fault zone falls within the expected range for optimally aligned fractures for strike-slip faults. The lower crustal shear strength results in less available shear stress which could explain why our stress drop estimates are lower compared to Onwuemeka *et al.* (2018), who measure stress drops in the range of ∼2–200 MPa for seismic events as deep as the boundary of the seismogenic zone, and Holmgren *et al.* (2019), who measure an average stress drop of 7.5 MPa at ∼4 km depth. If the fault plane is not aligned favourably with regional stresses then our average stress drop estimate may be too small to be explained by crustal shear strength alone and will need additional pore-fluid pressure, which can decrease effective stresses (Zoback 2009), and therefore decrease available crustal shear strength.

Some studies that analyse seismic data sets where additional pore-fluid is injected into the subsurface report a growing stress drop with distance (e.g., Allmann *et al.* 2011; Kwiatek *et al.* 2014) from the injection point or a lower stress drop proximal to the injection point compared to events farther away (Pearson 1981; Lengliné *et al.* 2014; Yu *et al.* 2020), although others (e.g., Clerc *et al.* 2016; Sumy *et al.* 2017) could not confirm such trends. Most of our events are between 100 and 600 m from their points of injection. Within a distance of 10–300 m from the point of injection, Allmann *et al.* (2011) observe a factor of 5 stress drop increase and Kwiatek *et al.* (2014) observe an increase from ∼1 to ∼60 MPa over a distance of ∼100–500 m. Therefore, given our data set shows seismicity over similar distance ranges we would expect to see a signal of increasing stress drop with distance. However, we observe no such trend.

When hydraulic fluid is pumped into the subsurface, the rock intactness and permeability will determine how quickly fluid migrates into the rock matrix. The diffusion rate will determine the rate at which the pore pressure front moves away from the injection point, and therefore whether we see a change in crustal shear strength, which some studies show is expressed as an increasing stress drop with distance from the injection point (e.g., Allmann *et al.* 2011; Kwiatek *et al.* 2014). One key difference to the Allmann *et al.* (2011) study is that seismic events analysed here occur within a few hours of each other and are mostly associated with the same stage of injection, compared to a more gradual occurrence of seismicity over several days steadily away from the injection point (Allmann *et al.* 2011).

Kwiatek *et al.* (2014) observe an increasing stress drop with distance from the point of injection in seismicity on a reactivated fault. The main difference in this study is that seismicity occurs over the entire distance range in a few hours compared to days. The observation of a growing stress drop with time and distance can be explained by the weaker crustal shear strength proximal to the point of injection relative to stronger crust that is farther away, where the pore pressure is lower. However, in this study, the observation of a constant stress drop over a fault zone hundreds of metres deep in a short time span requires a more abrupt physical mechanism. One explanation could be a better fault connectivity and/or larger permeability along the fault plane (e.g., a more dilated fault), such that fluid can migrate quickly along the fault plane. This makes our observations consistent with this hypothesis of the dependency between stress drop and crustal shear strength when additional pore fluid is added to the subsurface. The physical mechanism of a direct hydraulic connection is supported by Kettlety *et al.* (2019).

A similar study in both spatial and temporal character to seismicity observed here is the geothermal test carried out by Pearson (1981). They observe an increase in stress drop with distance from the injection point over ∼600 m and a 6 hr injection time period. Here, the events span a ∼7-hr time period, although most events occur in a 3-hr window. Given the similar spatio-temporal character of data in this data set to Pearson (1981) we expect stress drops to increase with distance from the injection point in this data set. One reason why we may not observe a stress drop increase could be the permeability difference: the granite at Fenton Hill has low permeability (Pearson 1981), whereas the Keg-River formation is reported as highly permeable (Adams & Eccles 2002) and the fractures are likely to extend to the nearest perforation in the overlying shale (Kettlety *et al.* 2019). Conceptually, the pore-pressure front could have developed quickly over a large distance along the fault in this study, which explains why the initial seismicity which expresses a planar structure just below the shale play and hundreds of metres deeper in the limestone formation, occurs simultaneously (Fig. S3). Once the entire fault has experienced an increase in pore pressure, seismic events happening later will not have a significantly different crustal shear strength, therefore we will not observe a stress drop difference over time or space. Similar observations are made by Sumy *et al.* (2017) in the case of wastewater injection, where fault planes required relatively little additional stress to fail because of previous injection which had lowered the effective stresses.

7 CONCLUSIONS

In this study, we first highlight the challenges associated with retrieving robust high frequency estimates of source parameters from 112 $-0.6 \leq M_w \leq 0.7$ microseismic events recorded by borehole geophone arrays at a pad within the Horn River basin, British Columbia. Of these events we calculate first order estimates of stress drop from 90 events. Our results show that borehole geophones are prone to high frequency resonances above 250 Hz, which are most likely caused by receiver side instrument effects. Bandwidth limitations, resonances and severe attenuation limit the ability to faithfully retrieve high frequency information and estimate attenuation models. Deeper stations along both borehole arrays are particularly prone to resonances and the effects of high frequency cut-offs.

From our best estimates of *P*-phase spectra recorded at one of the wells (the K-well), we determine Q_p using two different empirical methods. $Q_p = 180 \pm 40$ appears to provide the most realistic stress drop estimates. We calculate a mean stress drop of 1.6 ± 1.2 MPa, which broadly supports self-similar scaling down to $M_w = -0.6$. However, our estimates are smaller than other regional induced and tectonic studies, which can be explained by lower effective stresses and/or lower crustal shear strength. It is likely that our estimates represent a lower bound of what are larger estimates because the retrieved corner frequencies may be biased downwards due to high frequency challenges. Finally, we find no statistically significant correlations between stress drop and depth or distance from injection, which could be explained by hydraulic fluid communicating relatively quickly along fractured rock compared to slower diffusion in more intact rock.

ACKNOWLEDGEMENTS

We would like to thank the operator for providing the data and ESG Solutions Ltd., the contractor that acquired and processed the data. We thank Adam Baig, Alan Baird, Tom Kettlety, James Verdon, Joanna Holmgren and Mike Kendall for helpful discussions regarding the Horn River Basin data set. We would also like to thank Anna Stork, Anthony Butcher and Rebecca Harrington for useful discussions. AGK was supported by the Future Opportunities fund of the University of Bristol titled Natural Hazards:Seismic (grant no. 1953784) associated with EPSRC EP/N509619/1. MJW was supported by NERC (NE/R017956/1, EQUIPT4RISK). This research was also supported by the Bristol University Microseismic Projects (BUMPS). We thank the reviewers, editor and assistant editor for their very constructive feedback, which significantly improved the manuscript quality.

DATA AVAILABILITY

Data are proprietary and not currently available publicly. To aid replicability, we provide an open-access database of the new source parameters on Zenodo (Klinger & Werner 2021), accessible from doi.org/10.5281/zenodo.5603087. The results file includes event IDs, magnitudes, corner frequencies and stress drops of the 94 microseismic events analysed in Section 5.5, as well as their uncertainties.

REFERENCES

Abercrombie, R.E., 1995. Earthquake source scaling relationships from -1 to 5 using seismograms recorded at 2.5-km depth., *J. geophys. Res.,* **100**(B12), 24015–24036.

Abercrombie, R.E., 1997. Near-surface attenuation and site effects from comparison of surface and deep borehole recordings, *Bull. seism. Soc. Am.,* **87**(3), 731–744.

Abercrombie, R.E., 1998. A summary of attenuation measurements from borehole recordings of earthquakes: the 10 Hz transition problem, *Pure appl. Geophys.,* **153**(2–4), 475–487.

Abercrombie, R.E., 2015. Investigating uncertainties in empirical Green's function analusis of earthquake source parameters, *J. geophys. Res.,* **120,** 4263–4277.

Abercrombie, R.E., 2021. *Resolution and Uncertainties in Estimates of Earthquake Stress Drop and Energy Release, Phil. Trans. R. Soc., A.,* **379**(2196),.

Adams, J. & Eccles, D., 2002. Controls on fluid flow systems in northern Alberta as related to MVT mineralization: a contribution to the carbonate-hosted Pb-Zn (MVT) targeted geoscience initiative Alberta, EUB/AGS Geo-Note.

Aki, K. & Richards, P.G., 2002. *Quantitative Seismology,* 2nd edn, University Science Books .

Aki, K., Fehler, M. & Das, S., 1977. Source mechanism of volcanic tremor: fluid-driven crack models and their application to the 1963 kilauea eruption, *J. Volc. Geotherm. Res.,* **2**(3), 259–287.

Allen, R.V., 1978. Automatic earthquake recognition and timing from single traces, *Bull. seism. Soc. Am.,* **68**(5), 1521–1532.

Allmann, B.P. & Shearer, P.M., 2009. Global variations of stress drop for moderate to large earthquakes, *J. geophys. Res.,* **114**(1), 1–22 , doi:10.1029/2008JB005821.

Allmann, B. P.G., Goertz, A. & Wiemer, S., 2011. Stress drop variations of induced earthquakes at the Basel geothermal site, *Geophys. Res. Lett.,* **38,** 1–5.

Anderson, J.G., 1986. Implication of attenuation for studies of the earthquake source, *Earthq. Source Mech.,* **37,** 311–318.

Anderson, J.G. & Hough, S.E., 1984. A model for the shape of the Fourier amplitude spectrum of acceleration at high frequencies, *Bull. seism. Soc. Am.,* **74**(5), 1969–1993.

Baig, A., Urbancic, T., Viegas, G. & Karimi, S., 2012. Can small events (Mw <0) observed during hydraulic fracture stimulations initiate large events (Mw >0)?, *Leading Edge,* **31**(12), 1470–1474.

Baird, A.F., Kendall, J.M., Fisher, Q.J. & Budge, J., 2017. The role of texture, cracks, and fractures in highly anisotropic shales, *J. geophys. Res.,* **122**(12), 10 341–10 351.

Bell, J.S., 2015. In situ stress orientations and magnitudes in the Liard Basin of Western Canada, *Geological Survey of Canada,* **OpenFile70,** 1–410.

Bethmann, F., Deichmann, N. & Mai, P.M., 2012. Seismic wave attenuation from borehole and surface records in the top 2.5km beneath the city of Basel, Switzerland, *Geophys. J. Int.,* **190**(2), 1257–1270.

Brune, J.N., 1970. Tectonic stress and the spectra of seismic shear waves from earthquakes, *J. geophys. Res.,* **75**(26), 4997–5009.

Butcher, A., 2018. *Microseismology: Characteristics, Magnitudes and Shallow Crustal Effects,* University of Bristol.

Clarke, H., Eisner, L., Styles, P. & Turner, P., 2014. Felt seismicity associated with shale gas hydraulic fracturing: the first documented example in Europe, *Geophys. Res. Lett.,* **41**(23), 8308–8314.

Clerc, F., Harrington, R.M., Liu, Y. & Gu, Y.J., 2016. Stress drop estimates and hypocenter relocations of induced seismicity near Crooked Lake, Alberta, *Geophys. Res. Lett.,* **43**(13), 6942–6951.

Deichmann, N., 2017. Theoretical basis for the observed break in ML/MW scaling between small and large earthquakes, *Bull. seism. Soc. Am.,* **107**(2), 505–520.

Deichmann, N. & Giardini, D., 2009. Earthquakes Induced by the stimulation of an enhanced geothermal system below Basel (Switzerland), *Seismol. Res. Lett.,* **80**(5), 784–798.

Eaton, D.W., van der Baan, M., Birkelo, B. & Tary, J.B., 2014. Scaling relations and spectral characteristics of tensile microseisms: evidence for opening/closing cracks during hydraulic fracturing, *Geophys. J. Int.,* **196**(3), 1844–1857.

Eshelby, J.D., 1957. The determination of the elastic field of an ellipsoidal inclusion, and related problems, *Proc. R. Soc. Lond., A,* **241**(1226), 376–396.

Eyre, T.S., Eaton, D.W., Garagash, D.I., Zecevic, M., Venieri, M., Weir, R. & Lawton, D.C., 2019. The role of aseismic slip in hydraulic fracturing-induced seismicity, *Sci. Adv.,* **5**(8), 1–11.

Faber, K. & Maxwell, P.W., 1997. Geophone spurious frequency: what is it and how does it affect seismic data quality?, *Can. J. Explor. Geophys.,* **33**(1), 46–54.

Fornasini, P., 2008. *The Uncertainty in Physical Measurements: An Introduction to Data Analysis in the Physics Laboratory,* Springer Science & Business Media.

Gaiser, J.E., Fulp, T.J., Petermann, S.G. & Karner, G.M., 1988. Vertical seismic profile Sonde coupling, *Geophysics,* **53**(2), 206–214.

Goebel, T., Weingarten, M., Chen, X., Haffener, J. & Brodsky, E., 2017. The 2016 Mw5. 1 Fairview, Oklahoma earthquakes: evidence for long-range poroelastic triggering at > 40 km from fluid disposal wells, *Earth planet. Sci. Lett.,* **472,** 50–61.

Goebel, T. H.W. & Brodsky, E.E., 2018. The spatial footprint of injection wells in a global compilation of induced earthquake sequences, *Science,* **361**(6405), 899–904.

Gubbins, D., 2005. Time series analysis and inverse theory for geophysicists, *Technometrics,* **47**(3), 374 , doi:10.1198/tech.2005.s291.

Haldorsen, J.B., Johnson, D.L., Plona, T., Sinha, B., Valero, H.-P. & Winkler, K., 2006. Borehole acoustic waves, *Oilfield Rev.,* **18**(1), 34–43.

Hanks, B. Y. T.C., 1982. Fmax, *Bull. seism. Soc. Am.,* **72**(6), 1867–1879.

Hanks, T.C. & Kanamori, H., 1979. A moment magnitude scale, *J. geophys. Res.,* **84**(B5), 2348–2350.

Harrington, R.M., Kwiatek, G. & Moran, S.C., 2015. Self-similar rupture implied by scaling properties of volcanic earthquakes occurring during the 2004-2008 eruption of Mount St. Helens, Washington, *J. geophys. Res.,* **120**(7), 4966–4982.

Heidbach, O., Reinecker, J., Tingay, M., Müller, B., Sperner, B., Fuchs, K. & Wenzel, F., 2007. Plate boundary forces are not enough: Second- and third-order stress patterns highlighted in the World Stress Map database, *Tectonics,* **26**(6), 1–19.

Hiramatsu, Y., Yamanaka, H., Tadokoro, K., Nishigami, K. & Ohmi, S., 2002. Scaling law between corner frequency and seismic moment of microearthquakes: Is the breakdown of the cube law a nature of earthquakes?, *Geophys. Res. Lett.,* **29**(8), 52–1-52-4.

Holmgren, J.M. & Werner, M.J., 2021. Raspberry shake instruments provide initial ground-motion assessment of the induced seismicity at the united downs deep geothermal power project in Cornwall, United Kingdom, *Seismic Record,* **1**(1), 27–34.

Holmgren, J.M., Atkinson, G.M. & Ghofrani, H., 2019. Stress drops and directivity of induced earthquakes in the western Canada sedimentary basin, *Bull. seism. Soc. Am.,* **109**(5), 1635–1652.

Hough, S.E., 2014. Shaking from injection-induced earthquakes in the Central and Eastern United States, *Bull. seism. Soc. Am.,* **104**(5), 2619–2626.

Hua, W., Chen, Z. & Zheng, S., 2013. Source parameters and scaling relations for reservoir induced seismicity in the Longtan Reservoir Area, *Pure appl. Geophys.,* **170**(5), 767–783.

Huang, Y., Beroza, G.C. & Ellsworth, W.L., 2016. Stress drop estimates of potentially induced earthquakes in the Guy-Greenbrier sequence, *J. geophys. Res.,* **121,** 6597–6607.

Huang, Y., Ellsworth, W.L. & Beroza, G.C., 2017. Stress drops of induced and tectonic earthquakes in the central United States are indistinguishable, *Sci. Adv.,* **3**(August), 1–7.

Ide, S. & Beroza, G.C., 2001. Does apparent stress vary with earthquake size?, *Geophys. Res. Lett.,* **28**(17), 3349–3352.

Ide, S., Beroza, G.C., Prejean, S.G. & Ellsworth, W.L., 2003. Apparent break in earthquake scaling due to path and site effects on deep borehole recordings, *J. geophys. Res.,* **108**(B5) , doi:10.1029/2001JB001617.

Ide, S., Matsubara, M. & Obara, K., 2004. Exploitation of high-sampling Hi-net data to study seismic energy scaling: the aftershocks of the 2000 Western Tottori, Japan, earthquake, *Earth, Planets Space,* **56**(9), 859–871.

Imanishi, K., Ellsworth, W.L. & Prejean, S.G., 2004. Earthquake source parameters determined by the SAFOD Pilot Hole seismic array, *Geophys. Res. Lett.,* **31**(12), 3–7.

Keranen, K., Weingarten, M., Bekins, B. & Ge, S., 2014. Sharp increase in central Oklahoma seismicity since 2008 induced by massive wastewater injection, *Science,* **345**(6195), 448–451.

Kettlety, T., Verdon, J.P., Werner, M.J., Kendall, J.M. & Budge, J., 2019. Investigating the role of elastostatic stress transfer during hydraulic fracturing-induced fault activation, *Geophys. J. Int.,* 1200–1216.

Kettlety, T., Verdon, J.P., Werner, M.J. & Kendall, J.M., 2020. Stress transfer from opening hydraulic fractures controls the distribution of induced seismicity, *J. geophys. Res.,* **125**(1) , doi:10.1029/2019JB018794.

Klinger, A.G. & Werner, M.J., 2021. Microseismic source parameters from induced seismicity in the Horn river basin (British Columbia) [Dataset], Zenodo

Ktenidou, O.-J., Cotton, F., Abrahamson, N.A. & Anderson, J.G., 2014. Taxonomy of κ: a review of definitions and estimation approaches targeted to applications, *Seismol. Res. Lett.,* **85**(1), 135–146.

Kwiatek, G., Bulut, F., Bohnhoff, M. & Dresen, G., 2014. High-resolution analysis of seismicity induced at Berlín geothermal field, El Salvador, *Geothermics,* **52,** 98–111.

Lei, X., Huang, D., Su, J., Jiang, G., Wang, X., Wang, H., Guo, X. & Fu, H., 2017. Fault reactivation and earthquakes with magnitudes of up to Mw4.7 induced by shale-gas hydraulic fracturing in Sichuan Basin, China, *Scientific Reports,* **7**(1), 7971 , doi:10.1038/s41598-017-08557-y.

Lengliné, O., Lamourette, L., Vivin, L., Cuenot, N. & Schmittbuhl, J., 2014. Fluid-induced earthquakes with variable stress drop, *J. geophys. Res.,* **119**(12), 8900–8913.

Lin, Y.Y., Ma, K.F., Kanamori, H., Alex Song, T.R., Lapusta, N. & Tsai, V.C., 2016. Evidence for non-self-similarity of microearthquakes recorded at a Taiwan borehole seismometer array, *Geophys. J. Int.,* **206**(2), 757–773.

Lomax, A., Michelini, A. & Curtis, A., 2009. Earthquake location, direct, global-search methods, in *Encyclopedia of Complexity and Systems Science,* ed. Meyers, R., Springer, doi:10.1007/978-3-642-27737-5_150-2.

Madariaga, B. Y.R., 1976. Dynamics of an expanding circular fault, *Bull. seism. Soc. Am.,* **66**(3), 639–665.

McGarr, A., 1999. On relating apparent stress to the stress causing earthquake fault slip, *J. geophys. Res.,* **104**(B2), 3003–3011.

Moos, D. & Zoback, M.D., 1990. Utilization of observations of well bore failure to constrain the orientation and magnitude of crustal stresses: application to continental, Deep Sea Drilling Project, and Ocean Drilling Program boreholes, *J. geophys. Res.,* **95**(B6), 9305–9325.

Onwuemeka, J., Liu, Y. & Harrington, R.M., 2018. Earthquake stress drop in the Charlevoix Seismic Zone, Eastern Canada, *Geophys. Res. Lett.,* **45**(22), 12 226–12 235.

Pearson, C., 1981. The relationship between microseismicity and high pore pressures during hydraulic stimulation experiments in low permeability granitic rocks, *J. geophys. Res.,* **86,** 7855–7864.

Pettitt, W., Montes, J.R., Hemmings, B., Hughes, E., Young, R.P., *et al.*, 2009. Using continuous microseismic records for hydrofracture diagnostics and mechanics, in *Proceedings of the 2009 SEG Annual Meeting,* SEG Technical Program Expanded Abstracts: 1542-1546, Society of Exploration Geophysicists.

Podvin, P.& Lecomte, I., 1991. Finite difference computation of traveltimes in very contrasted velocity models: a massively parallel approach and its associated tools, *Geophys. J. Int.,* **105**(1), 271–284.

Prieto, G.A., Parker, R.L., Thomson, D.J., Vernon, F.L. & Graham, R.L., 2007. Reducing the bias of multitaper spectrum estimates, *Geophys. J. Int.,* **171**(3), 1269–1281.

Rubinstein, J.L. & Mahani, A.B., 2015. Myths and facts on wastewater injection, hydraulic fracturing, enhanced oil recovery, and induced seismicity, *Seismol. Res. Lett.,* **86**(4), 1060–1067.

Ruhl, C.J., Abercrombie, R.E. & Smith, K.D., 2017. Spatiotemporal variation of stress drop during the 2008 Mogul, Nevada, Earthquake Swarm, *J. geophys. Res.,* **122**(10), 8163–8180.

Sayers, C., Den Boer, L., Dasgupta, S. & Goodway, B., 2015. Anisotropy estimate for the Horn River Basin from sonic logs in vertical and deviated wells, *Leading Edge,* **34**(3), 296–306.

Shearer, P.M., Abercrombie, R.E., Trugman, D.T. & Wang, W., 2019. Comparing EGF methods for estimating corner frequency and stress drop from P wave spectra, *J. geophys. Res.,* **124**(4), 3966–3986.

Sleefe, G., Warpinski, N. & Engler, B.P., 1993. Observations of broadband micro-seisms during reservoir stimulation, in *Paper presented at the 1993 SEG Annual Meeting,* Washington, DC, September 26–30, Paper Number: SEG-1993-0263.

Sleefe, G., Warpinski, N., Engler, B., *et al.*, 1995. The use of broadband microseisms for hydraulic fracture mapping, *SPE Format. Eval.,* **10**(04), 233–240.

Streit, J.E., 1997. Low frictional strength of upper crustal faults: a model, *J. geophys. Res.,* **102**(11), 24 619–24 626.

Sumy, D.F., Neighbors, C.J., Cochran, E.S. & Keranen, K.M., 2017. Low stress drops observed for aftershocks of the 2011 Mw 5.7 Prague, Oklahoma, earthquake, *J. geophys. Res.,* **122**(5), 3813–3834.

Sun, R. & McMechan, G.A., 1988. Nonlinear reverse-time inversion of elastic offset vertical seismic profile data, *Geophysics,* **53**(10), 1295–1302.

Tan, Y. *et al.*, 2020. Hydraulic fracturing induced seismicity in the southern sichuan basin due to fluid diffusion inferred from seismic and injection data analysis, *Geophys. Res. Lett.,* **47**(4), 1–10.

Tary, J.B., van der Baan, M. & Eaton, D., 2014. Interpretation of resonance frequencies recorded during hydraulic fracturing treatments, *J. geophys. Res.,* **120,** 1195–1209.

Tomic, J., Abercrombie, R.E. & do Nascimento, A.F., 2009. Source parameters and rupture velocity of small M 2.1 reservoir induced earthquakes, *Geophys. J. Int.,* **179**(2), 1013–1023.

Trugman, D.T. & Shearer, P.M., 2017. Application of an improved spectral decomposition method to examine earthquake source scaling in Southern California, *J. geophys. Res.,* **122**(4), 2890–2910.

Vaezi, Y. & Van der Baan, M., 2014. Analysis of instrument self-noise and microseismic event detection using power spectral density estimates, *Geophys. J. Int.,* **197**(2), 1076–1089.

Van Der Baan, M., 2009. The origin of sh-wave resonance frequencies in sedimentary layers, *Geophys. J. Int.,* **178**(3), 1587–1596.

Venkataranman, A., Beroza, G.C., Ide, S., Imanishi, K., Ito, H. & Iio, Y., 2006. Measurements of spectral similarity for microearthquakes in western Nagano, Japan, *J. geophys. Res.,* **111**(3), 1–10.

Verdon, J.P. & Budge, J., 2018. Examining the capability of statistical models to mitigate induced seismicity during hydraulic fracturing of shale gas reservoirs, *Bull. seism. Soc. Am.,* **108**(2), 690–701.

Verdon, J.P., Kendall, J.-M., Stork, A.L., Chadwick, R.A., White, D.J. & Bissell, R.C., 2013. Comparison of geomechanical deformation induced by megatonne-scale CO_2 storage at Sleipner, Weyburn, and in Salah, *Proc. Natl. Acad. Sci.,* **110**(30), E2762–E2771.

Waldhauser, F. & Ellsworth, W.L., 2000. A double-difference earthquake location algorithm: method and application to the Northern Hayward Fault, California, *Bull. seism. Soc. Am.,* **90**(6), 1353–1368.

Wang, R., Gu, Y.J., Schultz, R. & Chen, Y., 2018. Faults and non-double-couple components for induced earthquakes, *Geophys. Res. Lett.,* **45**(17), 8966–8975.

Wu, Q. & Chapman, M., 2017. Stress-drop estimates and source scaling of the 2011 mineral, Virginia, mainshock and aftershocks, *Bull. seism. Soc. Am.,* **107**(6), 2703–2720.

Yaskevich, S., Duchkov, A.A. & Myasnikov, A., 2019. A case study on receiver-clamping quality assessment from the seismic-interferometry processing of downhole seismic noise recordings, *Geophysics,* **84**(3), B195–B203.

Yenier, E. & Atkinson, G.M., 2015. An equivalent point-source model for stochastic simulation of earthquake ground motions in California, *Bull. seism. Soc. Am.,* **105**(3), 1435–1455.

Yoon, S.H., Joe, Y.J., Koh, C.S., Woo, J.H. & Lee, H.S., 2018. Sedimentary processes and depositional environments of the gas-bearing Horn River shale in British Columbia, Canada, *Geosci. J.,* **22**(1), 33–46.

Yu, H., Harrington, R.M., Kao, H., Liu, Y., Abercrombie, R.E. & Wang, B., 2020. Well proximity governing stress drop variation and seismic attenuation associated with hydraulic fracturing induced earthquakes, *J. geophys. Res.,* **125**(9),.

Zhang, H., Eaton, D.W., Li, G., Liu, Y. & Harrington, R.M., 2016. Discriminating induced seismicity from natural earthquakes using moment tensors and source spectra, *J. geophys. Res.,* **121**(2), 972–993.

Zhang, Z., Rector, J.W. & Nava, M.J., 2018. Microseismic hydraulic fracture imaging in the Marcellus Shale using head waves, *Geophysics,* **83**(2), KS1–KS10.

Zoback, M.D., 2009. Rock failure in compression, tension and shear, in *Reservoir Geomechanics,* pp. 84–139, Cambridge Univ. Press.

SUPPORTING INFORMATION

Supplementary data are available at *GJI* online.

Figure S1: Histograms of stress drop estimates for the three crustal attenuation models we consider. (a) $Q = 110$, (b) $Q = 120$ and (c) $Q = 180$.

Figure S2: Demonstration of observed spectra, model fits and synthetic spectra from bootstrapping, from 2 example events. The corresponding histograms of residuals and modelled Gaussian distributions are shown in (b) and (d), for (a) and (c), respectively. (a and c) Displacement-amplitude spectra where red dashed lines shows the *P*-phase arrival. The black solid line shows the best model fit (circles showing the log spaced sample points for inversion) and the corresponding corner frequency is shown by a blue vertical line. Grey lines show the synthetic spectra from bootstrapping and the range of bootstrapped corner frequencies is shown by the grey patch. The black solid line shows the pre-event noise, where multitaper sample points are marked by a tick.

Figure S3: Injection rate and depth of seismic events against time in hours for events during and just after injection into stage A14. Each seismic event is shown by a circle corresponding to the depth (right *y*-axis). Grey circles show all seismic events recorded by the contractor and red circle show events used in this study. Blue line shows injection rate corresponding to stage A14 (left *y*-axis).

Please note: Oxford University Press is not responsible for the content or functionality of any supporting materials supplied by the authors. Any queries (other than missing material) should be directed to the corresponding author for the paper.